Pathophysiological remodeling of the skeletal muscle microenvironment in patients with lung cancer

Edmund Battey[1*], Andrea Irazoki[1*], Jakob Wang[2,3*], Jonas Sørensen[1,7], Johanne Louise Modvig[1], Scott Themsen[1], Christian Thomas Voldstedlund[5], Cathrine Knøs[1], Nicoline Resen Andersen[1], Emma Frank[1], Søren Kudahl[3], Nanna Hahn[1], Anna Madsen[1], Steffen H. Raun[1], Clara Prats[1,6], Oksana Dmitryev[4], Niels Ørtenblad[8], Jean Farup[2,3#], Lykke Sylow[1#]

1. Department of Biomedical Sciences, Faculty of Health and Medical Sciences, University of Copenhagen, Denmark.
2. Steno Diabetes Center Aarhus, Aarhus University Hospital, Aarhus, Denmark.
3. Department of Biomedicine, Aarhus University, Aarhus, Denmark.
4. Novo Nordisk Foundation Center for Basic Metabolic Research, Faculty of Health and Medical Sciences, University of Copenhagen, Copenhagen, Denmark
5. Department of Nutrition, Exercise and Sports, University of Copenhagen, Denmark.
6. The Core Facility for Integrated Microscopy, Faculty of Health and Medical Sciences, University of Copenhagen, Denmark
7. Department of Nephrology, Section of Palliative Medicine, Copenhagen University Hospital, Herlev-Gentofte, Denmark
8. Department of Sports Science and Clinical Biomechanics, University of Southern Denmark, Denmark

*These authors contributed equally.
#These authors jointly supervised this work.

Keywords: skeletal muscle atrophy, muscle microenvironment, fibroadipogenic progenitor, fat deposition, mitochondrial dysfunction, immune cell infiltration, lung cancer, cancer biology

Abstract

Cancer-associated cachexia is characterized by weight loss, muscle wasting, systemic inflammation, and functional decline. This multifactorial syndrome is highly prevalent and detrimental in patients with advanced-stage non–small cell lung cancer (NSCLC). To investigate the cellular and molecular underpinnings of muscle wasting, we analyzed skeletal muscle biopsies from NSCLC patients and healthy matched controls using quantitative proteomics, histology, fluorescence-activated cell sorting, gene expression profiling, and high-resolution respirometry. Skeletal muscle from patients was characterized by type II muscle fiber atrophy, greater collagen deposition, and redistribution of lipids to the extracellular matrix. This coincided with a shift in fibro-adipogenic progenitors (FAPs), favouring the $CD90^{-}$ subtype, and experiments using conditioned media indicated a catabolic secretory phenotype from patient-derived FAPs. Proteomic and functional analyses revealed dysregulated calcium handling, downregulation of key mitochondrial proteins, and altered respiratory capacity in muscle samples from patients with NSCLC. These alterations, along with fiber-type specific mitochondrial remodelling, were accompanied by STAT3 activation and immune cell infiltration, suggesting a link between mitochondrial dysfunction and local inflammation. These results provide the first human evidence that altered FAP composition, mitochondrial homeostasis, calcium handling, and immune cell landscape coincide with muscle wasting in NSCLC, highlighting potential therapeutic targets to treat patients with cancer-associated cachexia.

Introduction

Cancer-associated cachexia (CAC) is a multifactorial syndrome characterized by unintentional weight loss and skeletal muscle wasting, contributing to poor prognosis (Del Ferraro et al., 2012; Kimura et al., 2015; Lin et al., 2022; Martin et al., 2013). CAC affects 30-60 % of patients with non-small cell lung cancer (NSCLC) (Baracos et al., 2018). For these patients, loss of muscle mass and function severely impairs survival, tolerance to anticancer therapy, physical function, and quality of life (Christensen et al., 2014). Uncovering the molecular drivers of CAC-related muscle deterioration may enable the development of targeted therapies to improve treatment and survival.

Within the skeletal muscle niche, certain cellular and molecular alterations in muscle fibers and adjacent cell types are likely to drive atrophy and degeneration in CAC, while others act to preserve muscle mass and resist degeneration. Maintaining functional interactions between fibro-adipogenic progenitors (FAPs), muscle stem cells (MuSCs), and immune cells may be crucial for avoiding pathological remodelling in CAC (Evano & Tajbakhsh, 2018; Mitchell et al., 2010). FAPs are mesenchymal progenitor cells residing in the skeletal muscle with the capacity to differentiate into fibrogenic or adipogenic lineages depending on subcellular phenotype and the surrounding factors of the muscle microenvironment (Fitzgerald et al., 2023; Giuliani et al., 2022). Fibrosis is a common feature in rodent CAC muscle and has been found in patients with pancreatic cancer (Judge et al., 2018; Washington et al., 2023). Some evidence indicate a pro-fibrotic $CD90^+$ subpopulation of FAPs drive collagen production and muscle degeneration in type II diabetes (Farup et al., 2021) but its role in CAC is unknown. FAPs can also drive deposition of ectopic adipocytes in the extracellular matrix, which may directly contribute to the pathophysiology of CAC (Arrighi et al., 2015; Fitzgerald et al., 2023; Loumaye et al., 2015; Stephens et al., 2011). Furthermore, FAPs are emerging as crucial and targetable mediators of intercellular cross-talk within the muscle in health and disease (Fukada & Uezumi, 2023; Theret et al., 2021), with preclinical models emphasizing their contribution to muscle atrophy in sarcopenia and denervation (Madaro et al., 2018; Uezumi et al., 2021). However, to our knowledge, no human data currently exist the role of FAPs in driving skeletal muscle deterioration in CAC.

The presence of immune cells and a pro-inflammatory environment within skeletal muscle niche is key for remodelling and regeneration (Panci & Chazaud, 2021). Certain immune cell subsets positively correlate with muscle mass and muscle fiber size in patients with cancer (Anoveros-Barrera et al., 2019; Yu et al., 2024). On the other hand, through the chronic secretion of pro-inflammatory cytokines such as interleukin-6 (IL-6) and tumor necrosis factor-alpha (TNF-α), immune cells may promote catabolic pathways, induce apoptosis and inhibit muscle regeneration, contributing to the progression of CAC (Chang et al., 2023; He et al., 2013; Lemos et al., 2015).

An emerging field of study describes that primary mitochondrial dysfunctions can activate inflammatory signals (López-Armada et al., 2013; Marchi et al., 2023). In skeletal muscle, such mechanisms result in muscle atrophy and subsequent immune cell infiltration (Irazoki et al., 2022, 2023; Rodríguez-Nuevo et al., 2018; Sliter et al., 2018; Zhang et al., 2019). Mitochondrial dysfunctions can further lead to over production of reactive oxygen species (ROS) that results in protein and DNA damage, which can induce inflammatory responses and muscle atrophy (Agrawal et al., 2023; Marchi et al., 2023). In fact, various forms of mitochondrial dysfunction have been associated with ROS-mediated activation of inflammatory responses in both immune and non-immune cells (Manoharan et al., 2024; Riley & Tait, 2020). Vice versa, systemic inflammation also alters skeletal muscle mitochondrial function (Abad et al., 2024; Abid et al., 2020; Dasgupta et al., 2024), which in turn induce fibrosis and exacerbate muscle wasting. Several preclinical studies (Beltrà et al., 2021; VanderVeen et al., 2020) and a few human studies (Dolly et al., 2022; Kunz et al., 2022) have shown that CAC alters mitochondrial function. Yet, whether muscle atrophy could be linked to dysregulated mitochondrial function, alterations in subcellular FAP composition and function, ROS-triggered muscle inflammation, and immune cell infiltration remains unknown. Understanding the interplay between the muscle niche and mitochondrial function could provide molecular insights into therapeutic strategies aiming to attenuate local muscle inflammation and preserve muscle mass in patients with CAC. Moreover, asserting the association between molecules produced in the muscle mitochondria, such as ROS, and influx of inflammatory cells, may reveal novel mediators of local muscle inflammation.

Mass spectrometry (MS)–based proteomics have emerged as powerful tools for unbiased, system-wide quantifications, including broad proteome alterations of specific proteins or pathways (Aebersold & Mann, 2016). Unravelling the proteomic changes in skeletal muscle from patients with cancer could provide important new insights into molecular changes and elucidate new targets to prevent pathological remodelling in CAC. Yet, how CAC influences the cellular composition of the muscle microenvironment is unclear, and human molecular proteomics data is considerably lacking (Bentzinger et al., 2013; Rodríguez et al., 2024).

Here, using a combination of proteomics, fluorescence activated cell sorting, histological and biochemical analyses, together with *in vitro* experiments, we found that patients with advanced NSCLC displayed muscle atrophy, fibrosis and elevated extracellular matrix lipid deposition at the time of diagnosis, when compared to matched controls. In NSCLC, there were marked differences in the composition of FAP subpopulations compared with controls, and conditioned media from NSCLC-derived FAPs resulted in muscle atrophy in vitro. Altered mitochondrial function, oxidative stress and calcium dysregulations were associated with a shift towards an inflammatory phenotype on the protein level, as well as infiltration of specific immune cell subpopulations. Our results identify FAP, immune cell and mitochondrial alterations in skeletal muscle from patients with advanced stage NSCLC, highlighting

126 potential therapeutic targets to mitigate CAC in these patients. Moreover, we create a
127 first open-source muscle NSCLC Proteome dataset, representative of the population
128 of patients with NSCLC compared to well-matched controls, which offer mechanistic
129 insights into the pathophysiology of CAC.

Results

Skeletal muscle microenvironment structural and proteomic remodelling in patients with NSCLC

To determine structural remodelling of skeletal muscle in patients with NSCLC, we assessed muscle fiber cross-sectional area (CSA), lipid deposition and fibrosis in skeletal muscle biopsies from newly diagnosed NSCLC patients and weight- and sex matched controls. Baseline participant characteristics are included in Table 1.

Patients with NSCLC exhibited skeletal muscle atrophy, with reduced muscle fiber CSA compared to controls (Figure 1A-F, Supplementary Figure 1A). This was primarily driven by a 23.5% reduction in type II fiber CSA (Figure 1B). Notably, NSCLC muscle displayed a higher proportion of smaller type II fibers, with a similar trend observed in type I fibers, while fiber type proportions were similar between groups (Figure 1D and 1F, Supplementary Figure 1B).

In chronic diseases, such as muscular dystrophies and sarcopenia, muscle is known to accumulate ectopic fat and extracellular matrix constituents, known as fibro-fatty infiltration (Mann et al., 2011). We evaluated this process by quantifying muscle lipid content using BODIPY staining (Figure 1G). Our data demonstrate that patients with NSCLC had a redistribution of muscle lipids to the extracellular matrix (Figure 1H-I). While intramuscular lipid droplet area was similar between groups (Figure 1J), overall lipid content was lower in patients with NSCLC across both fiber types (Figure 1K, Supplementary Figure 1C). Additionally, we observed a trend towards increased Type I/Type II intensity ratio in NSCLC, suggesting a shift in intramyocellular lipid distribution to oxidative fibers (Supplementary Figure 1D). In contrast, we observed no differences in intramuscular glycogen deposition (Supplementary Figure 1E). Collagen deposition was greater in patients with NSCLC compared with controls (Figure 1L-M), revealing structural remodelling of skeletal muscle in response to NSCLC.

Having established structural remodelling of the muscle microenvironment in NSCLC, we next employed unbiased mass spectrometry (MS)-based global proteomics to comprehensively characterize molecular alterations associated with muscle atrophy in patients with NSCLC. We quantified a total of 3620 proteins, of which 897 were upregulated and 536 were downregulated in skeletal muscle from patients with NSCLC compared to controls (adjusted $P < 0.05$; Figure 1N). Principal component analysis indicated clear separation by condition (Supplementary Figure 1F).

Enrichment analysis highlighted extracellular matrix-related terms, as well as lipid binding and transport pathways, consistent with the histological observations (Figure 1O-P). Additionally, regulators of the ubiquitin-proteasome system (NEDD8, ATG7, FBXO7, UBR1), fibrosis and ECM remodelling (COL18A1, FGA, FGB, FGG, FN1; Vidal et al., 2008), and lipid metabolism (PLIN1, FASN, APOE, TECR) were upregulated in patients with NSCLC (Figure 1Q-S).

169 Interestingly, the muscle protein content of the atrophy-related genes (atrogenes)
170 ATROGIN1 and MuRF1, together with the autophagy marker P62, was similar
171 between patients with NSCLC and controls (Supplementary Figure 1G-I), in line with
172 findings from patients with gastric cancer (D'Orlando et al., 2014).

173 Collectively, these findings show that skeletal muscle atrophy associates with collagen
174 deposition and a redistribution of lipids to the extracellular matrix in patients with
175 NSCLC. Together with altered protein degradation, ECM remodelling and lipid
176 metabolism, these results highlight a structural and proteomic remodelling resulting in
177 fibro-fatty alterations of the skeletal muscle microenvironment and enrichment of
178 proteins involved in the regulation of proteolysis, protein neddylation, lipid binding, and
179 collagen-containing extracellular matrix that could contribute to CAC in patients with
180 NSCLC.

181 **Skeletal muscle of patients with NSCLC displays a greater proportion of CD90$^-$**
182 **FAPs, which induces atrophy in vitro**

183 To investigate possible drivers of the observed muscle atrophy and ECM remodelling
184 in NSCLC, we quantified, isolated and characterized FAPs and MuSCs using FACS
185 on skeletal muscle biopsies from a subgroup of patients and controls. Our results
186 showed a greater predominance of CD90$^-$ FAPs in NSCLC compared with controls
187 (Figure 2A). Interestingly, CD90$^-$ FAPs have previously been suggested to hold a
188 greater adipogenic differentiation potential compared to CD90$^+$ FAPs (Farup et al.,
189 2021). Additionally, CD90$^-$ FAPs showed a trend for greater cell size compared to
190 controls (Figure 2B). Overall FAP content and size were similar across groups (Figure
191 2C-D).

192 Furthermore, we assessed the ability of FAPs to enter the cell cycle by quantifying 5-
193 ethynyl-2'-deoxyuridine (EdU) incorporation *in vitro* post sorting (Supplementary
194 Figure 2). This analysis indicated similar propensity of NSCLC patient-derived FAPs
195 to enter the cell cycle compared to controls (Figure 2E-F). Since FAPs are known to
196 secrete trophic factors influencing muscle fiber size regulation (Fukada & Uezumi,
197 2023; Kaneshige et al., 2022; Lukjanenko et al., 2019; Madaro et al., 2018), we treated
198 C2C12 myotubes with FAP conditioned media from patients with NSCLC and controls
199 (Supplementary Figure 2). Strikingly, conditioned media from FAPs of NSCLC patients
200 reduced myotube width compared to controls, suggesting that differences in overall
201 FAP composition and/or phenotype may partially explain the myofiber atrophy
202 observed in patients with NSCLC (Figure 2G-H).

203 In addition to analyzing FAPs, we also investigated MuSC content, morphology and
204 proliferation capacity. In congruence with our observations in FAPs, no differences in
205 overall MuSC content were observed in the comparison between patients with NSCLC
206 and controls (Figure 2I). However, MuSC cell size was larger in NSCLC muscle
207 compared with controls (Figure 2J), which may indicate cellular stress or senescence
208 (Chadha et al., 2024; Neurohr et al., 2019). Meanwhile, we detected no marked
209 differences in the proliferation capacity of MuSCs between controls and patients with

210 NSCLC, suggesting preserved MuSC function in context of NSCLC, at least under ex
211 vivo conditions outside the native muscle environment (Figure 2K-L).

212 Overall, we show a greater proportion of CD90⁻ FAPs in NSCLC, highlighting a
213 potential contributor to ECM lipid deposition and fibro-fatty remodeling. Furthermore,
214 factors secreted by these FAPs induced myotube atrophy in vitro. Although MuSC
215 content and function appeared unaffected by NCSLC, the marked increase in MuSC
216 cell size could indicate cellular stress, which may impact regenerative dynamics within
217 the altered muscle microenvironment. Collectively, these data point to FAP-driven
218 myofiber atrophy as a likely contributor to the muscle remodeling seen in NSCLC.

219 **NSCLC skeletal muscle exhibits mitochondrial alterations**

220 We next investigated skeletal muscle processes that contribute to changes in the
221 skeletal muscle microenvironment. In this regard, mitochondrial dysfunction is known
222 to impact muscle atrophy, in part through muscle inflammation and infiltration of
223 immune cells (Irazoki et al., 2023; Rodríguez-Nuevo et al., 2018). Thus, leveraging the
224 proteomics dataset we assessed the mitochondrial proteome, mitochondrial
225 respiratory capacity and structural organization of skeletal muscles of patients with
226 NSCLC.

227 Enrichment analysis of proteins differentially regulated in patients with NSCLC
228 compared with controls revealed over-representation of terms related to mitochondria,
229 including aerobic respiration, mitochondrial organization, and mitochondrial translation
230 (Figure 3A, Supplementary Figure 3A). Among the proteins downregulated in NSCLC
231 skeletal muscle were COX8A, MRPL24, NNT and OXA1L, involved in mitochondrial
232 respiration, translation, redox balance and inner membrane structure, respectively
233 (Figure 3B).

234 To understand the functional consequences of these proteomic changes, we
235 characterized mitochondrial biology in muscle of patients with NSCLC. First, we
236 evaluated skeletal muscle mitochondrial oxygen consumption as a proxy for
237 mitochondrial respiratory capacity. Our data indicate unaltered oxygen consumption
238 in patients with NSCLC compared to controls, with the exception of increased CIV-
239 dependent O_2 consumption (Figure 3C). This was not associated with differences in
240 the protein levels of oxidative phosphorylation (OxPhos) subunit forming complexes
241 (Figure 3D, Supplementary Figure 3B) nor mitochondrial transcripts (Supplementary
242 Figure 3C). However, we detected a trend towards a decrease in protein content of
243 the mitochondrial transcription factor TFAM (Figure 3E, Supplementary Figure 3D),
244 which can impact mitochondrial DNA (mtDNA) stability and abundance, leading to
245 alterations in oxidative phosphorylation subunit content and respiratory capacity.

246 Because changes in respiratory capacity are dependent on mitochondrial mass, we
247 evaluated this parameter using several approaches. Gene expression analysis of the
248 mitochondrial biogenesis marker PGC1α (*PPARGC1a*) showed similar levels in
249 skeletal muscle of patients with NSCLC compared to controls (Supplementary Figure

250 3E). In contrast, we observed a reduction in protein levels of the mitochondrial
251 membrane proteins TOM20 and TIM44 in skeletal muscles of patients with NSCLC
252 compared to controls (Figure 3F, Supplementary Figure 3F), indicative of reductions
253 in mitochondrial mass (Xu et al., 2022). To corroborate these findings, we used
254 confocal imaging to quantify the mitochondrial fractional area as an estimate of
255 mitochondrial mass. Notably, we observed that, although controls exhibited lower
256 mitochondrial fractional area in type II fibers compared to type I fibers, this difference
257 was blunted in NSCLC (Figure 3G-H), suggesting fiber type-specific adaptations in
258 mitochondrial abundance in patients with NSCLC.

259 Control of mitochondrial morphology is also a crucial determinant of mitochondrial
260 function and prevention of muscle inflammation and atrophy (Irazoki et al., 2023;
261 Rodríguez-Nuevo et al., 2018). Although we did not observe differences in protein
262 content of mitochondrial fusion proteins Mitofusin 1 and 2 (MFN1, 2) and the master
263 regulator of fission DRP1 (Supplementary Figure 3G-H), we detected reduced
264 fragmentation in type II fibers in NSCLC compared to controls (Figure 3G and I) in line
265 with muscle atrophy primarily occurring in type II fibers. These data indicate fiber type-
266 specific alterations also at the level of mitochondrial network organization, which may
267 directly impact the oxidative capacity of muscle fibers.

268 Taken together, our results suggest relevant skeletal muscle mitochondrial
269 adaptations to NSCLC, with fiber type-specific changes in mitochondrial proteins,
270 mass and morphology with a slight increased CIV-dependent O_2 consumption.

271 **Mitochondrial oxidative stress and calcium dysregulation in NSCLC skeletal**
272 **muscle**

273 Our proteome analysis revealed enrichment in pathways related to oxidoreductase
274 activity and calcium ion transport between NSCLC and controls (Figure 4A). Among
275 mitochondrial redox regulators, thioredoxin 2 (TXN2) and peroxiredoxin 3 (PRDX3),
276 both involved in oxidative stress responses, were downregulated in NSCLC (Figure
277 4B). TNX2 is involved in redox signaling and muscle mass regulation (Nordberg &
278 Arnér, 2001; Tang et al., 2022), while PRDX3 plays a role in mitochondrial redox
279 homeostasis and supports muscle contractile function by scavenging hydrogen
280 peroxide (Ahn et al., 2022; Cox et al., 2009).

281 In contrast, we found that superoxide dismutase 3 (SOD3) and catalase (CAT) were
282 upregulated in NSCLC, suggesting enhanced ROS scavenging activity in the
283 extracellular matrix and peroxisomes (Figure 4B). SOD3 dismutates superoxide
284 radicals into hydrogen peroxide in the extracellular space and regulates MuSC
285 function (Nowaczyk et al., 2020; Zelko et al., 2002). CAT localizes in peroxisomes and
286 breaks down hydrogen peroxide, with reduced CAT activity associated with
287 sarcopenia (Chelikani et al., 2004; Sullivan-Gunn & Lewandowski, 2013).

288 To further investigate the contribution of mitochondrial oxidative stress in skeletal
289 muscle of patients with NSCLC, we evaluated intracellular compartmentalization of

290 oxidative stress by quantifying the dimerization ratio of peroxiredoxins (PRDX2 and
291 PRDX3), which reside in the cytosol and mitochondria, respectively. Under high
292 oxidative stress, PRDXs oxidize and dimerize (Supplementary Figure 4A). Our data
293 show that PRDX2 total levels and dimerization remained unaltered (Figure 4C-D,
294 Supplementary Figure 4B). However, PRDX3 total levels were decreased in NSCLC
295 compared to controls (Figure 4E, Supplementary Figure 4B), consistent with our
296 proteomic findings. Concomitantly, we observed an increased PRDX3 dimerization
297 ratio in NSCLC (Figure 4F, Supplementary Figure 4B), indicating elevated
298 mitochondrial oxidative stress.

299 Interestingly, the increased PRDX3 dimerization was not explained by enhanced
300 mitochondrial superoxide dismutase (SOD2) protein content (Supplementary Figure
301 4B-C), which could lead to increased mitochondrial H_2O_2. Furthermore, we found no
302 change in total H_2O_2 levels in skeletal muscle (Supplementary Figure 4D). These data
303 suggest the potential contribution of other mitochondrial redox species to the
304 dimerization of PRDX3.

305 In our proteome analysis, we found alterations in regulators of calcium homeostasis.
306 CAMK2A, a member of the calcium/calmodulin dependent-protein kinase II subfamily
307 located in the plasma membrane that transduces calcium-dependent signals, was
308 upregulated in NSCLC compared with controls (Figure 4B). We also detected
309 downregulation of mitochondrial porin VDAC2, a voltage-dependent anion channel
310 responsible for the transport of metabolites across the mitochondrial membrane,
311 including ions such as calcium (Shoshan-Barmatz & De, 2017). Lastly, the histidine-
312 rich calcium binding protein (HRC) is a regulator of SR calcium cycling (Arvanitis et
313 al., 2011) and was also downregulated in patients with NSCLC (Figure 4B). We
314 validated the former by immunoblotting the mitochondrial porin VDAC1 and observed
315 a decrease in its protein content in patients with NSCLC compared to controls (Figure
316 4G, Supplementary Figure 4E). Overall, these data indicated potential alterations at
317 the level of calcium homeostasis in the skeletal muscle of patients with NSCLC.

318 In skeletal muscle, the SR regulates calcium levels and in particular calcium release
319 and uptake during muscle contraction and relaxation. Thus, having identified
320 alterations in SR-related proteins, we next assessed SR function in relation to calcium
321 handling. We found a slower SR calcium uptake and reduced SR calcium release rate
322 in patients with NSCLC compared with controls (Figure 4H-I). Lower calcium uptake
323 and release rates occurred despite comparable protein levels of components of SR
324 calcium cycling machinery (SERCA 1/2, STIM1 or CSQ1) between patients with
325 NSCLC and controls, suggesting that the capacity or regulation of these proteins,
326 rather than their expression levels, may be altered (Figure 4J, Supplementary Figure
327 4E). Overall, these findings demonstrate impairments in the activity of SR and
328 alterations in proteins related to calcium handling in skeletal muscle in patients with
329 NSCLC, which is in line with our previous observations in a murine model of CAC
330 (Irazoki et al., 2025).

331 Together, our findings reveal increased oxidative stress restricted to mitochondria and
332 alterations in calcium regulation, both of which can contribute to the processes
333 involved in the development of muscle atrophy in patients with NSCLC.

334 **Enhanced Inflammatory and Immune Responses in NSCLC skeletal Muscle**

335 Having discovered alterations in FAPs proportions, mitochondrial function and redox
336 balance, which are potential inducers of muscle inflammation (Irazoki et al., 2023; Ji
337 et al., 2022), we next investigated the inflammation and immune cell landscape in
338 NSCLC skeletal muscle.

339 GO proteomic analyses revealed heightened immune and inflammatory responses in
340 the skeletal muscle of patients with NSCLC compared to controls, with upregulation of
341 proteins such as CRP, HP, ORM1, S100A8, and S100A9 (Figure 5A-B). Notably, the
342 complement factor C3 was also upregulated, consistent with the recent identification
343 of C3 as a potential mediator of inflammation-related atrophy in patients with
344 pancreatic cancer (D'Lugos et al., 2025). Importantly, we have demonstrated that
345 FAPs in elderly human skeletal muscle act as a local source of C3 (Brorson et al.,
346 2025). Given our observations on increased $CD90^-$ FAP predominance in NSCLC
347 skeletal muscle compared to controls, we evaluated whether these cells could be the
348 source of the increased C3 abundance. Single-cell RNA sequencing analyses showed
349 that $CD90^-$ FAPs exhibit enhanced C3 gene expression, compared to $CD90^+$ FAPs
350 (Supplementary Figure 5B), demonstrating a link between FAP subpopulation shifts
351 and inflammatory signaling in NSCLC.

352 NSCLC patients also exhibited increased plasma CRP and GDF-15 levels (Figure 5C-
353 D). To evaluate whether the skeletal muscle contributes to elevated plasma GDF-15
354 and pro-inflammatory cytokine levels in the context of NSCLC, we measured their
355 gene expression in muscle biopsies. These analyses showed a variety of expression
356 profiles within the NSCLC group, especially *IL6*, which included three patients with
357 approximately 2.5-fold increase compared to controls, one with 7.4-fold and one with
358 40-fold increase (Figure 5F). Interestingly, this latter patient also showed 2.2-fold and
359 5.9-fold increase in *IFNg* and *IL1b*, respectively. To evaluate a potential activation of
360 IL6 signalling in skeletal muscle in the context of NSCLC, we quantified protein content
361 of its downstream effectors NF-κB (its subunit P65) and STAT3 and its phosphorylated
362 state (pSTAT3). These assessments showed no changes between groups in P65 and
363 STAT3 total protein levels, although we detected a significant upregulation in pSTAT3
364 in patients with NSCLC (Figure 5G, Supplementary Figure 5A).

365 To dissect whether the increased abundance of pro-inflammatory proteins and
366 pSTAT3 was due to the triggering of cell-autonomous pro-inflammatory mechanisms
367 or to immune cell infiltration in the muscle, we performed immune cell profiling using
368 flow cytometry (Figure 5I). This analysis identified a trend towards an increased
369 infiltration of $CD45^+$ hematopoietic cells (Figure 5J). Within the myeloid compartment
370 ($CD45^+CD14^+$), we separated macrophages/monocytes according to their
371 inflammatory profile using $CD11c^{+/-}$ markers (Figure 5K-N; Jensen et al., 2021),

372 revealing no differences in macrophage polarization between groups. However,
373 skeletal muscle from patients with NSCLC had a greater lymphocyte content (Figure
374 5N), and relative cell quantification showed reduced macrophage-to-hematopoietic
375 cell ratio compared to controls (Figure 5O), while lymphocyte-to-hematopoietic cell
376 ratio remained unchanged (Figure 5P). These findings indicate a lymphoid bias with
377 the immune cell compartment in NSCLC skeletal muscle.

378 This altered immune profile is consistent with the increased pSTAT3 we observed and
379 aligns with previous studies showing that immune cell infiltration in patients with cancer
380 correlates with decreased muscle mass and altered muscle morphology (Anoveros-
381 Barrera et al., 2019; Yu et al., 2024). Moreover, the increased presence of
382 hematopoietic cells, alongside elevated content of $CD90^-$ FAPs (enriched in C3), could
383 indicate a role for FAPs in driving the altered inflammation in CAC, as recently reported
384 during muscle regeneration (Brorson et al., 2025).

385 Collectively, our data identify novel shifts in FAP and immune cell populations
386 associated with a pro-inflammatory muscle microenvironment characterized by
387 elevated STAT3 phosphorylation in patients with NSCLC, providing mechanistic
388 insight into the development of muscle wasting.

Discussion

Here, we comprehensively characterize skeletal muscle and its microenvironment in patients with advanced stage NSCLC, providing clinically relevant insights into proteomic rewiring and molecular alterations that could underlie the high propensity for muscle wasting and CAC. We reveal a multifaceted signature of cancer-associated muscle wasting that includes fibrosis, lipid redistribution, mitochondrial dysfunction, immune infiltration, and altered FAP populations. Importantly, we identify for the first time that FAP-secreted factors from patients with NSCLC directly induce myotube atrophy in vitro, implicating FAPs as active drivers of atrophy in human CAC. Together, these findings establish a unique human proteomic resource and highlight potential mechanisms contributing to muscle wasting and inflammation in CAC.

We found that NSCLC is associated with skeletal muscle wasting driven primarily by type II muscle fiber atrophy. This aligns with observations in rodent models of CAC (Alves et al., 2021; Roberts et al., 2013). In patients with various cancer types, muscle atrophy was observed in both type I and type II chemically skinned muscle fibers (Toth et al., 2016). Thus, fiber-type selective atrophy may be cancer-type specific. The preferential type II muscle fiber atrophy in NSCLC may be explained by greater susceptibility to proteolytic pathways (Anoveros-Barrera et al., 2019; Ciciliot et al., 2013; Yu et al., 2024). Our findings indicate that this phenomenon may be attributable to altered mitochondrial homeostasis, as evidenced by fiber type II-specific adaptations in mitochondrial network organization in patients with NSCLC.

In addition to muscle atrophy, we observed increased fibrosis and a redistribution of lipids toward the extracellular matrix in patients with NSCLC. Fibrosis has been implicated in muscle wasting in both patients with pancreatic cancer and preclinical models of lung cancer (Judge et al., 2018; Washington et al., 2023). The extracellular lipid accumulation we report builds upon previous observations that CAC is associated with reduced skeletal muscle density and fat infiltration into muscle tissue (Aubrey et al., 2014; Loumaye et al., 2015; Stephens et al., 2011). While earlier studies reported increased lipid droplet count or overall muscle fat content, our results demonstrate a reduction in total intramyocellular lipid content. This discrepancy may reflect methodological differences, as we directly quantified lipid droplets via immunohistochemistry, whereas prior studies relied on CT-derived radiodensity (Aubrey et al., 2014; Loumaye et al., 2015) or electron microscopy (Stephens et al., 2011). Additionally, we observed a trend toward an increased type I/type II BODIPY intensity ratio in NSCLC, suggesting a fiber type-specific shift in lipid distribution, potentially reflecting altered metabolic handling in oxidative fibers (Daemen et al., 2018). Taken together, these findings indicate that in NSCLC, lipids are redistributed toward the extracellular matrix, pointing to a potential fibro-adipogenic origin for this shift.

We hypothesize that the fibro-fatty remodelling observed in patients with NSCLC plays a role in the development of skeletal muscle atrophy and dysfunction (Zhang et

430 al., 2021). While overall FAP content was similar between groups, the shift towards
431 CD90$^-$ FAPs in patients with NSCLC could partly explain their predisposition towards
432 ECM fat deposition. We propose that the lipid deposition in NSCLC is driven by this
433 enrichment of pro-adipogenic CD90$^-$ FAPs, as specific FAP subpopulations have
434 been shown to contribute to fatty infiltration in muscle degeneration.

435 Previous pre-clinical studies have shown that FAP-derived factors crucially impact
436 muscle fiber homeostasis, partly through modulation of the local muscle environment
437 (Kaneshige et al., 2022; Lukjanenko et al., 2019). Importantly, our findings that
438 conditioned media from patient-derived FAPs induces myotube atrophy *in vitro*
439 mechanistically implicate FAPs as a local driver of muscle atrophy in CAC. The ability
440 of FAPs to reduce myotube size independently of direct immune or tumour cell
441 interaction suggests that they may autonomously induce muscle wasting in NSCLC.
442 Interestingly, these findings are in line with previous observations in preclinical models
443 of muscle wasting (Kajabadi et al., 2023) and muscle denervation (Madaro et al.,
444 2018). Targeting FAPs or their cell-derived paracrine mediators could therefore
445 provide a promising therapeutic avenue to prevent or attenuate muscle wasting in
446 NSCLC-associated CAC.

447 Together with a greater proportion of CD90$^-$ FAPs, we also observed immune cell
448 infiltration in the skeletal muscle of patients with NSCLC, which aligns with emerging
449 insights into FAP-mediated immune modulation during muscle regeneration. Pre-
450 clinical studies have revealed a striking cross-talk from FAPs to both macrophages
451 (Babaeijandaghi et al., 2023; Wosczyna et al., 2019) and muscle-resident T-cells
452 (Kuswanto et al., 2016). Recently, it has been demonstrated in aged human skeletal
453 muscle that FAPs are a local source of C3, a complement factor that supports
454 recruitment, survival, and phagocytic activity of pro-inflammatory macrophages during
455 regeneration (Brorson et al., 2025). Our proteomic analyses revealed increased
456 abundance of C3, together with other pro-inflammatory markers, such as CRP, HP,
457 S100A8 and S100A9, in the skeletal muscle of patients with NSCLC. This elevation of
458 C3 in NSCLC aligns with a recent report highlighting complement pathway activation
459 in skeletal muscle from pancreatic cancer-induced muscle wasting (D'Lugos et al.,
460 2025). Notably, our sequencing data from human skeletal muscle clearly
461 demonstrates enrichment of C3 transcripts in CD90$^-$ FAPs compared to CD90$^+$ FAPs.

462 Recent work identifying molecular subtypes in human skeletal muscle in CAC provides
463 strong support for our findings (Bhatt et al., 2025). In that study, RNAome analysis
464 revealed that patients in the cachexia-associated subtype had higher expression of
465 immune/cytokine storm pathways and extracellular matrix remodelling, with type IIA
466 and IIX fiber atrophy identified through histological analysis. Our study builds on and
467 complements these findings by providing the first proteomic evidence of increased
468 skeletal muscle abundance of complement component C3 and inflammatory
469 mediators such as CRP, HP, S100A8 and S100A9 in patients with NSCLC. Together,
470 these complementary transcriptomic and proteomic data provide converging evidence

471 that inflammation and complement activation are central features of the cachectic
472 muscle phenotype, reinforcing their potential as therapeutic targets.

473 We also observed elevated circulating levels of GDF-15, which has been implicated in
474 the anorexia component to CAC (Chang et al., 2023), while its direct effects on the
475 muscle remain unclear. Concomitantly, we detected increased pSTAT3, a major
476 intrinsic signal responsive to a wide range of cytoplasmic receptors, leading to immune
477 modulatory pathways (Yu et al., 2009). Interestingly, FAPs have been identified as the
478 cellular origin of increased pSTAT3 activation in preclinical models of denervation-
479 induced muscle atrophy through induction of the IL6 pathway (Madaro et al., 2018).
480 These data demonstrate the pro-inflammatory milieu of skeletal muscles of patients
481 with NSCLC, which can further contribute to the development of muscle atrophy.

482 Mitochondrial abnormalities have been implicated in CAC and muscle atrophy, with
483 preclinical and human studies suggesting that altered mitochondrial mass, distribution
484 and dysfunction exacerbate muscle wasting (de Castro et al., 2019; Dolly et al., 2022;
485 Kunz et al., 2022; Snoke et al., 2023). Our data show that patients with NSCLC
486 exhibited increased CIV-dependent oxygen consumption and type II fiber-specific
487 reductions in mitochondrial fragmentation and mass. Although reduced, and not
488 enhanced, complex IV activity is associated with muscle atrophy in a murine model of
489 spinal muscle atrophy (Chemello et al., 2023), and we speculate that the detected
490 increase in CIV-dependent oxygen consumption is a result of maladaptive
491 mechanisms that aim to overcome the metabolic demands of the muscle in the context
492 of NSCLC. In fact, elevated mitochondrial respiration has also been reported in *in vitro*
493 models of mitochondrial hyperfusion (Irazoki et al., 2023), which aligns with our
494 observations on decreased mitochondrial fragmentation in type II fibers of patients
495 with NSCLC. Furthermore, enhanced mitochondrial respiration has been widely
496 reported to overproduce ROS (Chemello et al., 2023), which highlights a potential link
497 between enhanced CIV-dependent oxygen consumption and increased mitochondrial
498 oxidative stress in muscles of patients with NSCLC. Furthermore, preclinical studies
499 have reported that TFAM deficiency results in enhanced oxygen consumption,
500 increased oxidative stress (Vernochet et al., 2012) and mitochondrial elongation (West
501 et al., 2015), which also resembles our observations, although the expression levels
502 of TFAM protein in patients with NSCLC remained statistically equivalent to controls.

503 The relationship between oxidative stress and muscle atrophy has been widely
504 reported, in line with our findings in NSCLC (Agrawal et al., 2023). In fact, our
505 proteomic analysis revealed differential regulation of antioxidant enzymes involved in
506 redox homeostasis, including the mitochondrial TXN2 and PRDX3, extracellular SOD3
507 and peroxisomal CAT. Reduced TXN2 expression in NSCLC may contribute to the
508 observed muscle atrophy, since overexpression of TXN2 has been shown to attenuate
509 age-related muscle loss through suppression of mitochondrial oxidative stress (Tang
510 et al., 2022). While total hydrogen peroxide (H_2O_2) levels remained unchanged, the
511 selective increase in PRDX3 dimerization suggests that alternative redox species may
512 be involved in triggering oxidative damage in skeletal muscles of patients with NSCLC.

513 Based on evidence reporting a direct link between mitochondrial dysfunction and
514 muscle inflammation, we hypothesized that such processes could be implicated in
515 NSCLC (Irazoki et al., 2022, 2023; Rodríguez-Nuevo et al., 2018; Sliter et al., 2018;
516 Zhang et al., 2019). Our results showed that gene expression of relevant cytokines
517 induced by skeletal muscle mitochondrial dysfunction remained unaltered in the
518 context of NSCLC, suggesting that the alterations observed in skeletal muscle
519 mitochondrial function of patients with NSCLC do not induce cell-autonomous
520 inflammation. Notably, altered redox balance can also induce inflammation (Bellanti et
521 al., 2023). In this regard, oxidative stress induced by H_2O_2 treatment leads to STAT3
522 phosphorylation in human lymphocytes (Carballo et al., 2023). STAT3 is
523 phosphorylated and translocated onto mitochondria upon exacerbated mitochondrial
524 ROS production induced by Complex I inhibition in human cultured cells (Mohammed
525 et al., 2020). More importantly, a study using a murine model for denervation-induced
526 muscle atrophy demonstrates that skeletal muscle ROS activates neutrophils and
527 attracts them to the tissue (Xiang et al., 2022), highlighting a direct link between
528 skeletal muscle oxidative stress and immune cell infiltration. Although immune cells
529 may exert both protective and deleterious effects in muscle (Anoveros-Barrera et al.,
530 2019; Xiang et al., 2022; Yu et al., 2024), we speculate that chronic mitochondrial
531 dysfunction and oxidative stress induced by NSCLC facilitate the deleterious effects
532 of chronic immune cell infiltration in the muscle, exacerbating the muscle inflammatory
533 and wasting phenotype. Given that mitochondrial dysfunction and inflammation form
534 a vicious cycle in CAC (Marchi et al., 2023), targeting oxidative stress may represent
535 a promising intervention to mitigate muscle loss in NSCLC.

536 Our data indicates disrupted calcium homeostasis at the SR and mitochondria in
537 patients with NSCLC. We observed downregulation of the mitochondrial calcium
538 transporters VDAC1 and 2, which may limit mitochondrial calcium buffering capacity,
539 contributing to chronically elevated cytosolic calcium levels and stressing
540 mitochondrial function (Baines et al., 2005; De Stefani et al., 2012; Shoshan-Barmatz
541 & Ben-Hail, 2012). Additionally, CAMK2A has been shown to be implicated in
542 denervation-mediated muscle atrophy (Zhang et al., 2023). Interestingly, our
543 proteomics data showed upregulation of CAMK2A in patients with NSCLC, which may
544 reflect a compensatory mechanism aimed at restoring calcium balance to counteract
545 atrophy mediated by dysregulation of the SR-mitochondrial interface (Chin, 2005;
546 Zhang et al., 2023). Indeed, our functional data show altered SR calcium uptake and
547 release in NSCLC, supporting impaired calcium cycling between the SR and
548 mitochondria. Disrupted calcium handling can lead to elevated cytosolic calcium,
549 which is known to activate catabolic pathways (e.g., calpains, NF-κB) and contribute
550 to oxidative stress and inflammation (Qaisar et al., 2021). Calcium-driven oxidative
551 stress and inflammation may drive the alterations in FAPs we observed, since redox
552 and inflammatory cues shape FAP fate and function (Yao et al., 2025). Thus, together
553 with mitochondrial dysfunction and redox imbalance, these calcium disturbances could
554 contribute to muscle atrophy and promote the inflammatory environment observed in
555 NSCLC skeletal muscle (Qaisar et al., 2021).

556 We identified alterations in FAPs, calcium handling, oxidative stress, inflammation,
557 and mitochondrial function in NSCLC, all of which are also modulated by exercise
558 (Collao et al., 2020; Smith et al., 2023). Consistent with this, structured exercise after
559 chemotherapy has been shown to improve both survival and functional outcomes in
560 patients with colon cancer (Courneya et al., 2025). Our findings raise the possibility
561 that exercise may confer part of this benefit by mitigating the highlighted
562 pathophysiological alterations the skeletal muscle microenvironment and thereby
563 improving outcomes in CAC. Taken together, these findings warrant future well-
564 controlled intervention studies to define how the muscle microenvironment responds
565 to exercise in individuals with cancer.

566 **Conclusion**

567 We provide novel insights into the complex interplay between cellular and molecular
568 changes underlying muscle atrophy and structural remodelling in patients with
569 NSCLC. Our analysis reveals shifts in FAP and immune cell subsets within the muscle
570 microenvironment, along with mitochondrial alterations, enhanced oxidative stress
571 and altered calcium handling. These interactions may drive muscle atrophy in patients
572 with NSCLC and highlight potential therapeutic targets for counteracting cancer-
573 associated muscle wasting.

Materials and Methods

Participants

Participant characteristics are described in Table 1. Within the first week after being diagnosed, patients with advanced stage NSCLC were included at the Department of Oncology, Copenhagen University Hospital – Rigshospitalet, Copenhagen, between August 2022 and October 2023. Inclusion criteria were: (1) age > 18 years, (2) pathologically confirmed NSCLC (3) referred for first-line palliative systemic anticancer therapy (4) having a staging/baseline computed tomography (CT) scan within 4 weeks of initiation of treatment, or a baseline scan planned within the first week of treatment, (5) being in Eastern Cooperative Oncology Group Performance Score (ECOG PS) 0-2, (5) having signed the informed consent form to the study. Exclusion criteria were: (1) any other known malignancy requiring active treatment, (2) palliative radiotherapy as primary treatment, (3) ECOG PS >2, (4) physical disabilities excluding physical testing, (5) inability to understand Danish, (6) inability to understand scoring systems/patient-reported outcome measures, (7) taking anti-coagulant therapy that could not be discontinued for the muscle biopsy. If the oncologist found a patient capable of receiving anticancer treatment, no other comorbidities were reason for exclusion. Patients were classified, according to self-reported weight loss over 6 months prior to their diagnoses as: CAC (more than 5% loss of stable body weight over the past 6 months), or a BMI less than 20 kg/m² and ongoing weight loss (WL) of more than 2%, or sarcopenia and ongoing WL of more than 2% but have not entered the refractory stage; pre-CAC (1-5% WL), or non-CAC (increase or up to 1% WL. Sarcopenia was defined as L3 CT-derived skeletal muscle index (SMI) (cm2/m2) < 43/41 for normal or underweight men/women and <53/41 for overweight and obese men/women) (Fearon et al., 2011; Martin et al., 2013). 18 non-cancer and weight-stable control subjects, matched for age-, sex-, BMI and co-morbidity, were also included.

Protocol, approvals and handling of data

The study was carried out in accordance with the Helsinki Declaration, approved by the Regional Scientific Ethical Committee of the Capital Region of Denmark (H-21035808), and registered at www.clinicaltrials.gov (NCT05307367). All clinical data has been stored in a Redcap server operated by the Capital Region of Denmark and in agreement with the European Union's General Data Protection Regulation (GDPR). For this a data transfer agreement was obtained (Jr.nr 22019423). Approval for the processing of data was given from the local institutional board (514-0685/22-3000). Written informed consent was obtained from each patient before participation.

Body composition

Body composition was obtained using a dual-energy X-ray absorptiometry (DXA) scan at the MuscleLab at Copenhagen University Hospital – Rigshospitalet.

Blood sample and muscle tissue collection

614 The day before the first systemic treatment was initiated and 12 weeks into first-line
615 treatment non-fasted blood samples were taken. Analyses were performed at the
616 Dept. of Clinical Biochemistry Copenhagen University Hospital - Rigshospitalet. In the
617 same first week of systemic treatment (median day 6), the patients were invited to the
618 oncological outpatient clinic after an overnight fast. Patients were urged not to do
619 exercise 48 hrs prior to their biopsy visit. Percutaneous biopsy of the left *vastus*
620 *lateralis* was obtained from the third most proximal aspect of the patella and the
621 inguinal fold under local anaesthetic (lidocaine without adrenalin 20mg/ml). A 6-mm
622 incision was made through the skin, fat, and down to fascia, and the biopsy needle (6
623 mm Bergström) was advanced past the fascia into the muscle. Suction was applied
624 and the tissue was excised.

625 **Muscle tissue processing**

626 All biopsies were rinsed in ice cold saline within 30 s after procedure, and within 1-2
627 min a portion of fresh *Vastus lateralis* was quickly snap frozen in liquid nitrogen and
628 stored at -70 ºC. Biopsies were pulverized using a Bessman type tissue pulverizer
629 (Cellcrusher kit) on dry ice.

630 To preserve and assess peroxiredoxin 2 and 3 (PRDX2 and 3) dimerization ratios and
631 H_2O_2 levels, a fresh portion of the muscle biopsy was incubated for 10 min in ice-cold
632 100 mM N-Ethylmaleimide (NEM) diluted in PBS. NEM was subsequently aspirated,
633 and the tissue snap frozen.

634 For RNA extraction, samples were homogenized in QIAzol lysis reagent (#79306
635 Qiagen) with three sterile ceramic beads and using the TissueLyser II bead mill
636 (Qiagen, USA) for 3 min at 30 Hz.

637 For protein extraction, tissues were homogenized in ice cold homogenization buffer
638 (10% glycerol, 1% NP-40, 20 mM sodium pyrophosphate, 150 mM NaCl, 50 mM
639 HEPES (pH 7.5), 20 mM β-glycerophosphate, 10 mM NaF, 2mM phenylmethylsulfonyl
640 fluoride (PMSF), 1 mM EDTA (pH 8.0), 2 mM Na_3VO_4, 10 µg/mL leupeptin, 10 µg/mL
641 aproptinin, 3 mM benzamidine, 100 mM NEM) with a steel bead using the TissueLyser
642 II bead mill (Qiagen, USA) for 1 min at 30 Hz.

643 For flow cytometry, 80-200 mg of the muscle biopsies were immediately submerged
644 in ice-cold Hams F10+ including bicarbonate and glutamine (#N6908, Sigma-Aldrich,
645 Denmark), 10% horse serum (#26050088, Gibco, Thermo Fisher, MA) and 1%
646 pen/strep (#15140122, Gibco, Thermo Fisher, MA) (wash-buffer). Samples were
647 maintained on ice until further processing (within 1 hour), based on a previously
648 described protocol (Billeskov et al., 2023). Single cell suspensions were obtained via
649 enzymatic digestion using 700 U/mL collagenase II (#46D16552, Worthington,
650 Lakewood, NJ) and 3.27 U7/mL dispase I (#04 942 078 001, Roche Diagnostics,
651 Basel, Switzerland). After the addition of enzymes, samples were placed in a 37 ºC
652 water bath for 60 minutes and triturated with a pipette every 20 minutes to aid
653 digestion. Enzymes were blocked through addition of wash-buffer, and the cell
654 suspension was triturated through a 18G sterile needle 5 times and filtered through

655 70-um cell strainer (#130-110-916, Miltenyi Biotech). Finally, the cell suspension was
656 centrifuged at 500 g for 5 min, before the supernatant was removed and the cell pellet
657 was resuspended in 500 uL of cryopreservation buffer (StemMACs, #130-109-558
658 Miltenyi Biotech) and stored at -150 ºC until the day of sorting. Prior to digestion, the
659 sample weight was recorded to enable normalization of absolute cell counts to tissue
660 weight.

661 **Mass spectrometry and proteomics**

662 Approximately 5–7 mg of skeletal muscle biopsy tissue was transferred to Twintec
663 plates for proteomic analysis using the Astral platform. Raw data were processed
664 without imputation of missing values prior to differential expression analysis to
665 minimize artificial variance. To account for multiple hypothesis testing, permutation-
666 based testing with 15,000 iterations was applied. Proteins with an adjusted $P < 0.05$
667 and an absolute $\log_2$ fold-change > 0.1 were taken forward for Gene Ontology (GO)
668 over-representation analysis. GO enrichment was performed in STRING (v12), using
669 all detected proteins in the dataset as the background. Log_2 fold-change values for
670 selected proteins were compared between NSCLC and control samples.

671 **Histology**

672 Muscle biopsies were embedded in optimal cutting temperature (OCT) compound and
673 cryosectioned at 8 µm thickness with fibers oriented perpendicular to the blade to
674 ensure accurate assessment of muscle fiber morphology and size (Battey et al., 2024).

675 For fiber typing and membrane delineation, sections were blocked in 5% donkey
676 serum and incubated with primary antibodies for 3 hours at room temperature
677 (Supplementary Table 1). Corresponding secondary antibodies were used: DyLight
678 488–conjugated anti–mouse IgG1 (Jackson #115-545-205), DyLight 405–conjugated
679 anti–mouse IgM (Jackson #715-475-020), and Alexa Fluor 568–conjugated anti–rabbit
680 (Invitrogen #A11011). Nuclei were counterstained with Sytox™ Deep Red (1:2000).
681 Imaging was performed on a Carl Zeiss AxioObserver microscope through a Plan-
682 Apochromat 20x/0.8 objective.

683 To assess lipid accumulation, sections were fixed in methanol-free 4% formaldehyde
684 (Thermo Fisher Scientific #28908) for 20 minutes, followed by incubation with 0.5 µM
685 BODIPY™ 493/503 (Invitrogen #D3922) and Sytox™ Deep Red nuclear stain (1:2000;
686 Invitrogen #S11380) for 30 minutes at room temperature. Images were acquired using
687 a Carl Zeiss AxioObserver microscope through a Plan-Apochromat 20x/0.8 objective.

688 Collagen content was evaluated using the Picrosirius Red staining kit (Abcam
689 #ab150681). Sections were fixed in 4% formaldehyde for 20 minutes, washed in
690 distilled water, and stained with Sirius Red for 60 minutes. Excess dye was removed
691 by washing in 0.5% acetic acid, followed by dehydration, xylene clearing, and
692 mounting in Pertex. Brightfield and polarized light images were acquired using the Carl
693 Zeiss AxioScan 7, through a Plan-Apochromat 10x/0.45 objective.

694 Glycogen deposition was assessed performing periodic acid-Schiff (PAS) staining.
695 Fresh frozen muscle sections were fixed in 4% formaldehyde for 20 minutes and then
696 processed for PAS staining according to the manufacturer's protocol (395B-KT,
697 Sigma-Aldrich, Søborg, Denmark). The sections were treated with periodic acid
698 solution for 5 minutes. After sequential washes in running tap water and distilled water,
699 they were stained with Schiff reagent for 15 minutes, followed by an additional wash
700 in running tap water. Finally, the sections were dehydrated, cleared with xylene, and
701 mounted using Pertex. Brightfield images were acquired using a Zeiss AxioObserver
702 microscope by a blinded investigator.

703 Quantification of collagen and lipid deposition was done with QuPath software
704 (Bankhead et al., 2017). The fractional area of polarized signal (Picrosirius Red) was
705 measured by thresholding and normalizing it to the whole-tissue section. Lipid content
706 was analyzed by thresholding the BODIPY-positive pixels in five fields per section,
707 and fiber-specific signal intensity was quantified from 50–100 randomly chosen
708 individual fibers using Fiji (Schindelin et al., 2012). Membrane-to-cytosol lipid stain
709 intensity ratios were calculated by thresholding (MinError) laminin-defined membranes
710 and generating region of interests, which were transferred to the lipid images for
711 intensity measurements. Muscle fiber cross-sectional area and fiber type distribution
712 were determined using the Cellpose extension in QuPath on whole-section images
713 based on MyHC staining profiles.

714 **Myosin Heavy Chain composition analysis**

715 Myosin heavy chain isoform composition was analysed in muscle biopsy samples
716 using large-format SDS-PAGE to achieve high-resolution separation of isoforms.
717 Muscle homogenates were prepared and loaded in duplicate lanes at two different
718 protein concentrations to ensure linear detection. Samples were electrophoresed on
719 6% polyacrylamide gels under denaturing conditions for 68 h at low voltage, allowing
720 clear resolution of I, IIA and IIX isoforms. Gels were subsequently coomassie-stained,
721 and band intensities were quantified densitometrically. The relative abundance of each
722 MHC isoform was expressed as a percentage of total myosin heavy chain content.

723 **Respirometry**

724 A portion of fresh muscle was placed in ice-cold BIOPS solution (OROBOROS
725 Instruments, Innsbruck, Austria) immediately after dissection. Muscle fibers were
726 mechanically separated with needles on ice. Fibers were then permeabilized with 50
727 µg/mL saponin for 30 min on ice with shaking, followed by two 10 min washes in
728 MIRO5 respiration medium (OROBOROS Instruments, Innsbruck, Austria).
729 Approximately 2-3 mg of muscle fibers were transferred to the oxygraph-2k
730 (OROBOROS Instruments, Innsbruck, Austria) containing MIRO5 respiration medium.
731 Respiration measurements were performed at 37 ºC in hyperoxia ([O_2: 200-450
732 µmol/L). The protocol included adding 10 mM glutamate, 2 mM malate, and 5 mM
733 sodium pyruvate to assess resting respiration (state II, leak respiration), followed by
734 2.5 mM ADP for state III. Succinate at 10 mM was added to measure full electron
735 transport chain (ETC) capacity, upon which complexes I and III were inhibited by

736 adding 0.5 μM rotenone and 2.5 μM antimycin A. Then, ascorbate 2 mM and TMPD
737 0.5 mM were added to measure complex IV-dependent oxygen consumption.

738 **Single fiber isolation and immunostaining**

739 Skeletal muscle biopsy samples were fixed in Zamboni buffer (2% paraformaldehyde
740 supplemented with 1.2% picric acid) for 30 min at room temperature, followed by 4
741 hours in fresh fixative at 4 °C (Dahl et al., 2015). Biopsies were then dissected into
742 bundles of 10–20 fibres, transferred to 1:1 PBS/glycerol (v/v) for 1-3 days, and stored
743 at −20 °C. Fibers were further dissected into bundles of approximately 2-5 fibers. After
744 permeabilizing the muscle fibers with 0.2% Triton x100 and blocking non-specific
745 binding sites with 5% goat serum and, muscle fibers were stained to visualize type I
746 fibers and mitochondria, using with primary antibodies that detect Myosin Heavy Chain
747 7 (Developmental Studies Hybridoma Bank, AB_10572253) and COXIV (Abcam,
748 ab16056), respectively. The organization of intermyofibrillar mitochondria was
749 determined by thresholding the COXIV signal in ImageJ (Schindelin et al., 2012).
750 Mitochondrial fractional area (%) was determined by calculating the area of the region
751 of interest occupied by the COXIV signal divided by the total area of the region of
752 interest. Fragmentation index was calculated by dividing the number of mitochondrial
753 objects by the area of the mitochondria signal. 17.7 ± 3.8 fibers were analyzed per
754 biopsy by a blinded investigator.

755 **Gene expression analyses**

756 *Gene expression in skeletal muscle biopsies*

757 RNA was extracted using the RNeasy Mini Kit (Qiagen #74106) per the manufacturer's
758 instructions. RNA purity was assessed with the NanodropTM 2000/20000c
759 spectrometer and ND1000 software (ThermoFisher Scientific). Reverse transcription
760 was performed with 4 μL of qScript Ultra SuperMix (#95217, Quantabio) per 500 ng of
761 RNA. Gene expression was quantified by real-time quantitative PCR using SYBR
762 green (Applied Biosystems) and the QuantStudio 6 and 7 Real-Time PCR System
763 (Applied Biosystems), following the default comparative Ct protocol. Measurements
764 were normalized to a housekeeping gene (*RPLP0*). Primers and their sources are
765 listed in Supplementary Table 2.

766 *Single-cell RNAseq (10x Genomics)*

767 Single cell gene expression data was obtained from our publicly available dataset
768 deposited at the European Genome Archive (EGA number: EGAD00001008126).
769 Detailed description of the sequencing procedures are previously reported elsewhere
770 (Farup et al., 2021).

771 **Muscle H_2O_2 quantification**

772 The Amplex™ Red Hydrogen Peroxide/Peroxidase Assay Kit (Thermo Fisher) was
773 used following the manufacturer's indications.

774 **Immunoblotting**

775 After tissue homogenization for protein extraction, samples were rotated end-over-end
776 for 30 min at 4 ºC, then centrifuged at 13000 x g for 15 min at 4 ºC. Supernatants were
777 collected and stored at -80 ºC. Protein concentration was measured using the BCA
778 method (Thermo Fisher #23225) with BSA as standard (Sigma-Aldrich #P0834).
779 Protein extracts were resolved in 7%, 10%, or 12.5% Mini-PROTEAN precast
780 acrylamide gels (BioRad) for SDS-PAGE, transferred to PVDF membranes, and
781 blocked in TBS-Tween 20 with 2% milk protein for 5 min at room temperature.
782 Membranes were incubated with primary antibodies overnight at 4 ºC, followed by
783 HRP-conjugated secondary antibodies for 45 min at room temperature. Pierce™
784 Reversible Stain (Thermo Fisher #24585) was used as loading control. Bands were
785 visualized using the Bio-Rad ChemiDoc MP Imaging System and ECL+ (Amersham
786 Biosciences). Band densitometry was performed with Quantity One (Bio-Rad) and
787 bands were related to their own protein staining to correct for uneven loading. Primary
788 antibodies are listed in Supplementary Table 1. When analyzing dimerization ratios of
789 PRDX2 and PRDX3, protein extracts were prepared in the absence of the reducing
790 agent DTT.

791 **Calcium uptake and release assays**

792 Calcium uptake and release rates in sarcoplasmic reticulum (SR) vesicles were
793 measured using a fluorescent dye technique. Whole tissue homogenates were
794 prepared from frozen specimens using a Potter–Elvehjem glass homogenizer (Kontes
795 Glass Industry, Vineland, NJ) in an ice-cold buffer at a wet weight-to-volume ratio of
796 1:10. The buffer composition included 300 mM sucrose, 1 mM EDTA, 10 mM NaN_3,
797 40 mM Tris base, and 40 mM L-histidine, adjusted to pH 7.8, as described in detail
798 elsewhere (Gejl et al., 2014; Ørtenblad et al., 2011). Calcium levels were measured
799 using the fluorescent indicator Indo-1 (1 μM) at a sampling frequency of 20 Hz with a
800 Ratiomaster RCM system (Photon Technology International, Brunswick, NJ, USA).
801 Calcium uptake supported by oxalate was initiated by the addition of 2 mM ATP to
802 reach a final concentration of 5 mM. Uptake was recorded for approximately 3 minutes
803 until calcium levels plateaued below 100 nM, with no significant differences in plateau
804 observed between groups.

805 The SR calcium uptake rate, referred to as Tau, was defined as the time constant of
806 the single-exponential fit (the time required for free calcium concentration to decline
807 by 63%, equivalent to 1/e of the initial value) (Baylor & Hollingworth, 2003). Uptake
808 rates were also determined at two calcium concentrations: 400 nM (high) and 200 nM
809 (low), corresponding to muscle activation and resting levels of calcium. Following
810 uptake measurements, cyclopiazonic acid was used to inhibit the SR calcium ATPase
811 to estimate vesicular calcium leak. SR calcium release was then triggered by the
812 addition of 4-Chloro-m-cresol (5 mM).

813 Calcium data were mathematically analyzed using monoexponential curve fitting
814 (Curve Fitting Toolbox version 1.1.1; The MathWorks, Natick, MA, USA), as previously
815 described (Ørtenblad et al., 2011). Calcium uptake and release rates are expressed

816 in relative terms as nmol calcium per gram wet weight per minute (nmol·g^{-1} ww·min^{-1}).
817 Tau is expressed reciprocally (s^{-1}·g^{-1} ww), with higher values indicating faster calcium
818 reuptake. All SR assays were conducted in duplicate, performed by blinded
819 investigator, and the results were averaged.

820 **Plasma GDF-15 and CRP measurements**

821 Fasting blood samples were drawn at 10 am on biopsy days. A 9 ml dry tube stood for
822 a minimum of 30 min and maximum 1 hour at room temperature. Samples were then
823 spun down at 2000×g for 10 min at 4°C. 500 μl serum was aliquoted and stored at -
824 80°C. Plasma GDF-15 concentration was measured using a Human GDF-15
825 Quantikine ELISA kit (R&D Systems, #DGD150).

826 Plasma C-reactive protein (CRP) concentrations were analyzed using a latex particle–
827 based immunoassay (turbidimetry) on a Cobas 8000 analyzer (c702 module, Roche
828 Diagnostics). The method is standardized against the certified reference material
829 ERM-DA474/IFCC, with a measurement range of 1–700 mg/L and a reference interval
830 of <10 mg/L.

831 **Fluorescence activated cell sorting (FACS)**

832 On days of cell sorting, frozen vials with the single cell suspensions were briefly
833 thawed in a 37°C water bath and transferred to tubes containing 10 mL of wash buffer.
834 Each vial was washed three times to optimize cell yield, before the tube was
835 centrifuged at 500 g for 5 min at room temperature. Following aspiration of the
836 supernatant, samples were resuspended in 150 µL wash buffer containing a mixture
837 of antibodies (Supplementary Table 1).

838 Samples were protected from light to avoid bleaching and incubated during mild
839 agitation for 30 minutes at 5°C. Following incubation, the antibody mixture was diluted
840 with 15 mL wash buffer and centrifuged at 500 g for 5 minutes at RT. The supernatant
841 was removed, and the pellet was resuspended in 900 µL wash buffer prior to being
842 transfered into 5 mL FACS tubes through 30 µm cell strainers. Cells remained on ice
843 and were protected from light until FACS analysis.

844 Immediately before sorting propidium iodide and counting beads were added to each
845 sample, for assessment of cell viability and absolute cell counts, respectively. Samples
846 were briefly vortexed before sorting to loosen any precipitate. Sorting was performed
847 on the Bigfoot cell sorter (Thermo Fisher Scientific) using the 100 µm nozzle at 20 PSI
848 to minimize cellular strain. Flow data were collected in the Sasquatch software and
849 subsequently analyzed using FlowJo (version 10.6.2), with the gating strategy being
850 ascertained using fluorescence minus one controls. Freshly isolated FAPs and MuSCs
851 were collected in wash buffer and plated for in vitro experiments as outlined below.

852 ***In vitro* studies**

853 For assessment of proliferation capacity of FAPs and MuSCs, we utilized the EdU
854 incorporation assay as previously described (Farup et al., 2021). Freshly isolated
855 FAPs and MuSCs were seeded in 96-well half area plates (Corning, NY) pre-coated

with ECM (ECM gel, #E1270, Sigma). Cells were seeded at an appx. density of 10000 and 6000 cells/well in case of FAPs and MuSCs, respectively. Cells were seeded in 180 uL of wash-buffer including 10 uM of the EdU nucleotide. Hereafter, cells were left in the incubator untouched until the time fixation; three and five days following FACS in case of MuSCs and FAPs, respectively. Prior to fixation (4% PFA for 5 minutes) the media was collected and stored at -80 ºC until further used in conditioned-media experiments as described below. The wells were scanned using the EVOS M7000 imaging system (Thermo Fisher Scientific), and stitched images covering the entire well were then used to quantify the proportion of proliferating cells using ImageJ (NIH).

To investigate the potential effect of secreted factors from FAPs on myotube size regulation, we utilized conditioned media from the EdU-experiments in a C2C12-derived myotube cell culture. Here, C2C12 myoblasts (#91031101, Sigma Aldrich, passage 18) were seeded at 3000 cells/well in 96 well plates following cell expansion in a T75 culture flask. Cells were then grown into appx. 70-80% confluency in high glucose (4.5 g/L) DMEM including 20% fetal bovine serum and 1% pen/strep, prior to initiation of differentiation by serum starvation using 2% horse serum in low-glucose DMEM. Media was changed every other day for 12 days. During the 48 hours of FAP media exposure the differentiation media supplemented with 50% conditioned media from the EdU-culture, with a replenishment of the media following the first 24 hours of incubation. Following fixation, myotubes were stained for myosin heavy chain (MF20) and counterstained with DAPI. Images were acquired of the entire well using the EVOS M700 automated imaging system (Thermo Fisher Scientific). Myotube size was assessed as the average diameter of three randomly selected measurements along the length of each myotube, and the mean myotube diameter in each well was based on normalization to the amount of myotubes quantified. Only myotubes that were entirely visible within each field of view were eligible for analyses. All analysis of myotube size was performed by the same, blinded investigator using ImageJ (Schindelin et al., 2012).

Statistics

Data were collected using Excel 2016 and analyzed with GraphPad Prism 10.1.1 for Windows (GraphPad Software) and R Studio (v4.3.1). Data are expressed as mean ± SE, including individual values where applicable. Significance was set at $\alpha=0.05$, with $p<0.05$ shown. Data distribution was assessed using Shapiro–Wilk tests. Ordinary one-way ANOVA with Tukey's post-hoc test was used for comparing one variable across more than two groups. Two-way ANOVA with Tukey's post-hoc test was used for comparing multiple variables across both groups. Student's T-test or Mann-Whitney tests were used to compare one variable between both groups. Log2FC comparisons between groups were made using a Welch's t-test while permutation was applied to adjust for multiple comparisons. Data plots were generated with GraphPad Prism 10.1. 1. and R Studio.

Acknowledgements

We thank Professor Erik Richter and Betina Bolmgren for carrying out plasma GDF-15 analysis. We acknowledge the Core Facility for Integrated Microscopy, Faculty of Health and Medical Sciences, University of Copenhagen. We also thank the Proteomics Research Infrastructure (PRI), University of Copenhagen, for their support in performing the proteomic analyses for this study. Finally, we thank the FACS Core unit at Department at Biomedicine, Aarhus University for providing the necessary equipment for flow-based analyses. This work was supported by a research grant from the Danish Diabetes and Endocrine Academy (postdoctoral fellowship to E.B.), which is funded by the Novo Nordisk Foundation, grant number NNF22SA0079901.

Competing interests

The authors declare no competing interests.

Author contribution statements

Conceptualization: E.B., A.I., JW., J.S, J.F., and L.S. Data curation: E.B., A.I., J.W., C.T.V., N.Ø., J.F., and L.S. Formal analysis: E.B., A.I., J.W., J.S., C.T.V., J.L.M., S.T., O.D., N.Ø., S.K., J.F., and L.S. Funding acquisition: J.S., J.F., and L.S. Investigation: E.B., A.I., J.W., J.S., C.T.V., J.L.M., S.T., C.R.K., N.R.A., E.F., S.K., N.H., A.M., S.H.R., C.P., O.D., N.Ø., J.F., L.S. Methodology: E.B., A.I., J.W., J.S., C.T.V., C.P., O.D., N.Ø., J.F., and L.S. Project administration: E.B., A.I., J.W., J.S., J.F. and L.S. Resources: J.S., J.F., and L.S. Software: E.B., A.I., J.W., C.T.V., O.D., N.Ø., and J.F. Supervision: J.F. and L.S. Validation: E.B., A.I., J.W., J.S., C.T.V., J.L.M., O.D., N.Ø., J.F., and L.S. Visualization: E.B., A.I., J.W., O.D., and C.T.V. Writing original draft: E.B. and A.I. Writing review & editing: all authors.

References

Abad, C., Pinal-Fernandez, I., Guillou, C., Bourdenet, G., Drouot, L., Cosette, P., Giannini, M., Debrut, L., Jean, L., Bernard, S., Genty, D., Zoubairi, R., Remy-Jouet, I., Geny, B., Boitard, C., Mammen, A., Meyer, A., & Boyer, O. (2024). IFNγ causes mitochondrial dysfunction and oxidative stress in myositis. *Nature Communications*, *15*(1), 5403. https://doi.org/10.1038/s41467-024-49460-1

Abid, H., Ryan, Z. C., Delmotte, P., Sieck, G. C., & Lanza, I. R. (2020). Extramyocellular interleukin-6 influences skeletal muscle mitochondrial physiology through canonical JAK/STAT signaling pathways. *The FASEB Journal*, *34*(11), 14458–14472. https://doi.org/10.1096/fj.202000965RR

Aebersold, R., & Mann, M. (2016). Mass-spectrometric exploration of proteome structure and function. *Nature*, *537*(7620), 347–355. https://doi.org/10.1038/nature19949

Agrawal, S., Chakole, S., Shetty, N., Prasad, R., Lohakare, T., & Wanjari, M. (2023). Exploring the Role of Oxidative Stress in Skeletal Muscle Atrophy: Mechanisms and Implications. *Cureus*, *15*(7), e42178. https://doi.org/10.7759/cureus.42178

Ahn, B., Ranjit, R., Kneis, P., Xu, H., Piekarz, K. M., Freeman, W. M., Kinter, M., Richardson, A., Ran, Q., Brooks, S. V., & Van Remmen, H. (2022). Scavenging mitochondrial hydrogen peroxide by peroxiredoxin 3 overexpression attenuates contractile dysfunction and muscle atrophy in a murine model of accelerated sarcopenia. *Aging Cell*, *21*(3), e13569. https://doi.org/10.1111/acel.13569

Alves, C. R. R., Eichelberger, E. J., das Neves, W., Ribeiro, M. A. C., Bechara, L. R. G., Voltarelli, V. A., de Almeida, N. R., Hagen, L., Sharma, A., Ferreira, J. C. B., Swoboda, K. J., Slupphaug, G., & Brum, P. C. (2021). Cancer-induced muscle

943 atrophy is determined by intrinsic muscle oxidative capacity. *The FASEB Journal*,
944 *35*(7), e21714. https://doi.org/10.1096/fj.202100263R
945 Anoveros-Barrera, A., Bhullar, A. S., Stretch, C., Dunichand-Hoedl, A. R., Martins, K. J.
946 B., Rieger, A., Bigam, D., McMullen, T., Bathe, O. F., Putman, C. T., Field, C. J.,
947 Baracos, V. E., & Mazurak, V. C. (2019). Immunohistochemical phenotyping of T
948 cells, granulocytes, and phagocytes in the muscle of cancer patients:
949 Association with radiologically defined muscle mass and gene expression.
950 *Skeletal Muscle*, *9*(1), 24. https://doi.org/10.1186/s13395-019-0209-y
951 Arrighi, N., Moratal, C., Clément, N., Giorgetti-Peraldi, S., Peraldi, P., Loubat, A.,
952 Kurzenne, J.-Y., Dani, C., Chopard, A., & Dechesne, C. A. (2015).
953 Characterization of adipocytes derived from fibro/adipogenic progenitors
954 resident in human skeletal muscle. *Cell Death & Disease*, *6*(4), e1733–e1733.
955 https://doi.org/10.1038/cddis.2015.79
956 Arvanitis, D. A., Vafiadaki, E., Sanoudou, D., & Kranias, E. G. (2011). Histidine-Rich
957 Calcium Binding Protein: The New Regulator of Sarcoplasmic Reticulum
958 Calcium Cycling. *Journal of Molecular and Cellular Cardiology*, *50*(1), 43–49.
959 https://doi.org/10.1016/j.yjmcc.2010.08.021
960 Aubrey, J., Esfandiari, N., Baracos, V. E., Buteau, F. A., Frenette, J., Putman, C. T., &
961 Mazurak, V. C. (2014). Measurement of skeletal muscle radiation attenuation
962 and basis of its biological variation. *Acta Physiologica*, *210*(3), 489–497.
963 https://doi.org/10.1111/apha.12224
964 Babaeijandaghi, F., Kajabadi, N., Long, R., Tung, L. W., Cheung, C. W., Ritso, M., Chang,
965 C.-K., Cheng, R., Huang, T., Groppa, E., Jiang, J. X., & Rossi, F. M. V. (2023).
966 DPPIV+ fibro-adipogenic progenitors form the niche of adult skeletal muscle

967 self-renewing resident macrophages. *Nature Communications*, *14*(1), 8273.
968 https://doi.org/10.1038/s41467-023-43579-3
969 Baines, C. P., Kaiser, R. A., Purcell, N. H., Blair, N. S., Osinska, H., Hambleton, M. A.,
970 Brunskill, E. W., Sayen, M. R., Gottlieb, R. A., Dorn, G. W., Robbins, J., &
971 Molkentin, J. D. (2005). Loss of cyclophilin D reveals a critical role for
972 mitochondrial permeability transition in cell death. *Nature*, *434*(7033), 658–662.
973 https://doi.org/10.1038/nature03434
974 Bankhead, P., Loughrey, M. B., Fernández, J. A., Dombrowski, Y., McArt, D. G., Dunne,
975 P. D., McQuaid, S., Gray, R. T., Murray, L. J., Coleman, H. G., James, J. A., Salto-
976 Tellez, M., & Hamilton, P. W. (2017). QuPath: Open source software for digital
977 pathology image analysis. *Scientific Reports*, *7*(1), 16878.
978 https://doi.org/10.1038/s41598-017-17204-5
979 Baracos, V. E., Martin, L., Korc, M., Guttridge, D. C., & Fearon, K. C. H. (2018). Cancer-
980 associated cachexia. *Nature Reviews Disease Primers*, *4*(1), 1–18.
981 https://doi.org/10.1038/nrdp.2017.105
982 Battey, E., Dos Santos, M., Biswas, D., Maire, P., & Sakamoto, K. (2024). Protocol for
983 muscle fiber type and cross-sectional area analysis in cryosections of whole
984 lower mouse hindlimbs. *STAR Protocols*, *5*(4), 103424.
985 https://doi.org/10.1016/j.xpro.2024.103424
986 Baylor, S. M., & Hollingworth, S. (2003). Sarcoplasmic reticulum calcium release
987 compared in slow-twitch and fast-twitch fibres of mouse muscle. *The Journal of*
988 *Physiology*, *551*(1), 125–138. https://doi.org/10.1111/j.1469-7793.2003.00125.x
989 Bellanti, F., Lo Buglio, A., Quiete, S., Dobrakowski, M., Kasperczyk, A., Kasperczyk, S., &
990 Vendemiale, G. (2023). Sarcopenia Is Associated with Changes in Circulating

Markers of Antioxidant/Oxidant Balance and Innate Immune Response. *Antioxidants*, *12*(11), Article 11. https://doi.org/10.3390/antiox12111992

Beltrà, M., Pin, F., Ballarò, R., Costelli, P., & Penna, F. (2021). Mitochondrial Dysfunction in Cancer Cachexia: Impact on Muscle Health and Regeneration. *Cells*, *10*(11), 3150. https://doi.org/10.3390/cells10113150

Bentzinger, C. F., Wang, Y. X., Dumont, N. A., & Rudnicki, M. A. (2013). Cellular dynamics in the muscle satellite cell niche. *EMBO Reports*, *14*(12), 1062–1072. https://doi.org/10.1038/embor.2013.182

Bhatt, B. J., Ghosh, S., Mazurak, V., Brun, A. Q., Bathe, O., Baracos, V. E., & Damaraju, S. (2025). Molecular subtypes of human skeletal muscle in cancer cachexia. *Nature*, 1–10. https://doi.org/10.1038/s41586-025-09502-0

Billeskov, T. B., Jensen, J. B., Jessen, N., & Farup, J. (2023). Fluorescence-activated cell sorting and phenotypic characterization of human fibro-adipogenic progenitors. *STAR Protocols*, *4*(1), Article 1. https://doi.org/10.1016/j.xpro.2022.102008

Brorson, J., Lin, L., Wang, J., Bæk, A., Billeskov, T. B., Thybo, F. F., Just, J., Haskó, J., Ravn, C., Hansen, R. L., Bue, M., Jørgensen, J. O. L., Luo, Y., Jessen, N., & Farup, J. (2025). Complementing muscle regeneration—Fibro-adipogenic progenitor and macrophage-mediated repair of elderly human skeletal muscle. *Nature Communications*, *16*(1), 5233. https://doi.org/10.1038/s41467-025-60627-2

Carballo, M., Conde, M., El Bekay, R., Martín-Nieto, J., Camacho, M. J., Monteseirín, J., Conde, J., Bedoya, F. J., & Sobrino, F. (2023). Oxidative stress triggers STAT3 tyrosine phosphorylation and nuclear translocation in human lymphocytes. *The Journal of Biological Chemistry*, *274*(25), 17580–17586. https://doi.org/10.1074/jbc.274.25.17580

Chadha, Y., Khurana, A., & Schmoller, K. M. (2024). Eukaryotic cell size regulation and its implications for cellular function and dysfunction. *Physiological Reviews*, *104*(4), 1679–1717. https://doi.org/10.1152/physrev.00046.2023

Chang, K.-V., Wu, W.-T., Chen, Y.-H., Chen, L.-R., Hsu, W.-H., Lin, Y.-L., & Han, D.-S. (2023). Enhanced serum levels of tumor necrosis factor-α, interleukin-1β, and -6 in sarcopenia: Alleviation through exercise and nutrition intervention. *Aging (Albany NY)*, *15*(22), 13471. https://doi.org/10.18632/aging.205254

Chelikani, P., Fita, I., & Loewen, P. C. (2004). Diversity of structures and properties among catalases. *Cellular and Molecular Life Sciences CMLS*, *61*(2), 192–208. https://doi.org/10.1007/s00018-003-3206-5

Chemello, F., Pozzobon, M., Tsansizi, L. I., Varanita, T., Quintana-Cabrera, R., Bonesso, D., Piccoli, M., Lanfranchi, G., Giacomello, M., Scorrano, L., & Bean, C. (2023). Dysfunctional mitochondria accumulate in a skeletal muscle knockout model of Smn1, the causal gene of spinal muscular atrophy. *Cell Death & Disease*, *14*(2), 1–13. https://doi.org/10.1038/s41419-023-05573-x

Chin, E. R. (2005). Role of Ca2+/calmodulin-dependent kinases in skeletal muscle plasticity. *Journal of Applied Physiology*, *99*(2), 414–423. https://doi.org/10.1152/japplphysiol.00015.2005

Christensen, J. F., Jones, L. W., Andersen, J. L., Daugaard, G., Rorth, M., & Hojman, P. (2014). Muscle dysfunction in cancer patients. *Annals of Oncology*, *25*(5), 947–958. https://doi.org/10.1093/annonc/mdt551

Ciciliot, S., Rossi, A. C., Dyar, K. A., Blaauw, B., & Schiaffino, S. (2013). Muscle type and fiber type specificity in muscle wasting. *The International Journal of Biochemistry & Cell Biology*, *45*(10), 2191–2199. https://doi.org/10.1016/j.biocel.2013.05.016

Collao, N., Farup, J., & De Lisio, M. (2020). Role of Metabolic Stress and Exercise in Regulating Fibro/Adipogenic Progenitors. *Frontiers in Cell and Developmental Biology*, *8*. https://doi.org/10.3389/fcell.2020.00009

Courneya, K. S., Vardy, J. L., O'Callaghan, C. J., Gill, S., Friedenreich, C. M., Wong, R. K. S., Dhillon, H. M., Coyle, V., Chua, N. S., Jonker, D. J., Beale, P. J., Haider, K., Tang, P. A., Bonaventura, T., Wong, R., Lim, H. J., Burge, M. E., Hubay, S., Sanatani, M., ... Booth, C. M. (2025). Structured Exercise after Adjuvant Chemotherapy for Colon Cancer. *New England Journal of Medicine*, *393*(1), 13–25. https://doi.org/10.1056/NEJMoa2502760

Cox, A. G., Winterbourn, C. C., & Hampton, M. B. (2009). Mitochondrial peroxiredoxin involvement in antioxidant defence and redox signalling. *Biochemical Journal*, *425*(2), 313–325. https://doi.org/10.1042/BJ20091541

Daemen, S., Gemmink, A., Brouwers, B., Meex, R. C. R., Huntjens, P. R., Schaart, G., Moonen-Kornips, E., Jörgensen, J., Hoeks, J., Schrauwen, P., & Hesselink, M. K. C. (2018). Distinct lipid droplet characteristics and distribution unmask the apparent contradiction of the athlete's paradox. *Molecular Metabolism*, *17*, 71–81. https://doi.org/10.1016/j.molmet.2018.08.004

Dahl, R., Larsen, S., Dohlmann, T. L., Qvortrup, K., Helge, J. W., Dela, F., & Prats, C. (2015). Three-dimensional reconstruction of the human skeletal muscle mitochondrial network as a tool to assess mitochondrial content and structural organization. *Acta Physiologica*, *213*(1), 145–155. https://doi.org/10.1111/apha.12289

Dasgupta, D., Mahadev Bhat, S., Creighton, C., Cortes, C., Delmotte, P., & Sieck, G. C. (2024). Molecular mechanisms underlying TNFα-induced mitochondrial

fragmentation in human airway smooth muscle cells. *American Journal of Physiology. Lung Cellular and Molecular Physiology*, *326*(2), L190–L205. https://doi.org/10.1152/ajplung.00198.2023

de Castro, G. S., Simoes, E., Lima, J. D. C. C., Ortiz-Silva, M., Festuccia, W. T., Tokeshi, F., Alcântara, P. S., Otoch, J. P., Coletti, D., & Seelaender, M. (2019). Human Cachexia Induces Changes in Mitochondria, Autophagy and Apoptosis in the Skeletal Muscle. *Cancers*, *11*(9), 1264. https://doi.org/10.3390/cancers11091264

De Stefani, D., Bononi, A., Romagnoli, A., Messina, A., De Pinto, V., Pinton, P., & Rizzuto, R. (2012). VDAC1 selectively transfers apoptotic Ca2+ signals to mitochondria. *Cell Death and Differentiation*, *19*(2), 267–273. https://doi.org/10.1038/cdd.2011.92

Del Ferraro, C., Grant, M., Koczywas, M., & Dorr-Uyemura, L. A. (2012). Management of Anorexia-Cachexia in Late-Stage Lung Cancer Patients. *Journal of Hospice & Palliative Nursing*, *14*(6), 397. https://doi.org/10.1097/NJH.0b013e31825f3470

D'Lugos, A. C., Ducharme, J. B., Callaway, C. S., Trevino, J. G., Atkinson, C., Judge, S. M., & Judge, A. R. (2025). Complement pathway activation mediates pancreatic cancer-induced muscle wasting and pathological remodeling. *The Journal of Clinical Investigation*. https://doi.org/10.1172/JCI178806

Dolly, A., Lecomte, T., Tabchouri, N., Caulet, M., Michot, N., Anon, B., Chautard, R., Desvignes, Y., Ouaissi, M., Fromont-Hankard, G., Dumas, J.-F., & Servais, S. (2022). Pectoralis major muscle atrophy is associated with mitochondrial energy wasting in cachectic patients with gastrointestinal cancer. *Journal of Cachexia, Sarcopenia and Muscle*, *13*(3), 1837–1849. https://doi.org/10.1002/jcsm.12984

1087 D'Orlando, C., Marzetti, E., François, S., Lorenzi, M., Conti, V., di Stasio, E., Rosa, F.,
1088 Brunelli, S., Doglietto, G. B., Pacelli, F., & Bossola, M. (2014). Gastric cancer
1089 does not affect the expression of atrophy-related genes in human skeletal
1090 muscle. *Muscle & Nerve*, *49*(4), 528–533. https://doi.org/10.1002/mus.23945
1091 Evano, B., & Tajbakhsh, S. (2018). Skeletal muscle stem cells in comfort and stress. *Npj*
1092 *Regenerative Medicine*, *3*(1), 1–13. https://doi.org/10.1038/s41536-018-0062-3
1093 Farup, J., Just, J., de Paoli, F., Lin, L., Jensen, J. B., Billeskov, T., Roman, I. S., Cömert,
1094 C., Møller, A. B., Madaro, L., Groppa, E., Fred, R. G., Kampmann, U., Gormsen, L.
1095 C., Pedersen, S. B., Bross, P., Stevnsner, T., Eldrup, N., Pers, T. H., ... Jessen, N.
1096 (2021). Human skeletal muscle CD90+ fibro-adipogenic progenitors are
1097 associated with muscle degeneration in type 2 diabetic patients. *Cell*
1098 *Metabolism*, *33*(11), Article 11. https://doi.org/10.1016/j.cmet.2021.10.001
1099 Fearon, K., Strasser, F., Anker, S. D., Bosaeus, I., Bruera, E., Fainsinger, R. L., Jatoi, A.,
1100 Loprinzi, C., MacDonald, N., Mantovani, G., Davis, M., Muscaritoli, M., Ottery, F.,
1101 Radbruch, L., Ravasco, P., Walsh, D., Wilcock, A., Kaasa, S., & Baracos, V. E.
1102 (2011). Definition and classification of cancer cachexia: An international
1103 consensus. *The Lancet Oncology*, *12*(5), 489–495.
1104 https://doi.org/10.1016/S1470-2045(10)70218-7
1105 Fitzgerald, G., Turiel, G., Gorski, T., Soro-Arnaiz, I., Zhang, J., Casartelli, N. C.,
1106 Masschelein, E., Maffiuletti, N. A., Sutter, R., Leunig, M., Farup, J., & De Bock, K.
1107 (2023). MME+ fibro-adipogenic progenitors are the dominant adipogenic
1108 population during fatty infiltration in human skeletal muscle. *Communications*
1109 *Biology*, *6*(1), 1–21. https://doi.org/10.1038/s42003-023-04504-y

Fukada, S.-I., & Uezumi, A. (2023). Roles and Heterogeneity of Mesenchymal Progenitors in Muscle Homeostasis, Hypertrophy, and Disease. *Stem Cells (Dayton, Ohio)*, *41*(6), 552–559. https://doi.org/10.1093/stmcls/sxad023

Gejl, K. D., Hvid, L. G., Frandsen, U., Jensen, K., Sahlin, K., & Ørtenblad, N. (2014). Muscle glycogen content modifies SR Ca2+ release rate in elite endurance athletes. *Medicine and Science in Sports and Exercise*, *46*(3), 496–505. https://doi.org/10.1249/MSS.0000000000000132

Giuliani, G., Rosina, M., & Reggio, A. (2022). Signaling pathways regulating the fate of fibro/adipogenic progenitors (FAPs) in skeletal muscle regeneration and disease. *The FEBS Journal*, *289*(21), 6484–6517. https://doi.org/10.1111/febs.16080

He, W. A., Berardi, E., Cardillo, V. M., Acharyya, S., Aulino, P., Thomas-Ahner, J., Wang, J., Bloomston, M., Muscarella, P., Nau, P., Shah, N., Butchbach, M. E. R., Ladner, K., Adamo, S., Rudnicki, M. A., Keller, C., Coletti, D., Montanaro, F., & Guttridge, D. C. (2013). NF-κB–mediated Pax7 dysregulation in the muscle microenvironment promotes cancer cachexia. *The Journal of Clinical Investigation*, *123*(11), 4821–4835. https://doi.org/10.1172/JCI68523

Irazoki, A., Frank, E., Pham, T. C. P., Braun, J. L., Ehrlich, A. M., Haid, M., Riols, F., Hansen, C. H. F., Jørgensen, A.-S. R., Andersen, N. R., Hidalgo-Corbacho, L., Meneses-Valdes, R., Ali, M. S., Raun, S. H., Modvig, J. L., Gallero, S., Larsen, S., Gerhart-Hines, Z., Jensen, T. E., … Sylow, L. (2025). Housing Temperature Impacts the Systemic and Tissue-Specific Molecular Responses to Cancer in Mice. *Journal of Cachexia, Sarcopenia and Muscle*, *16*(2), e13781. https://doi.org/10.1002/jcsm.13781

1133 Irazoki, A., Gordaliza-Alaguero, I., Frank, E., Giakoumakis, N. N., Seco, J., Palacín, M.,
1134 Gumà, A., Sylow, L., Sebastián, D., & Zorzano, A. (2023). Disruption of
1135 mitochondrial dynamics triggers muscle inflammation through interorganellar
1136 contacts and mitochondrial DNA mislocation. *Nature Communications*, *14*(1),
1137 108. https://doi.org/10.1038/s41467-022-35732-1
1138 Irazoki, A., Martinez-Vicente, M., Aparicio, P., Aris, C., Alibakhshi, E., Rubio-Valera, M.,
1139 Castellanos, J., Lores, L., Palacín, M., Gumà, A., Zorzano, A., & Sebastián, D.
1140 (2022). Coordination of mitochondrial and lysosomal homeostasis mitigates
1141 inflammation and muscle atrophy during aging. *Aging Cell*, *21*(4), e13583.
1142 https://doi.org/10.1111/acel.13583
1143 Jensen, J. B., Møller, A. B., Just, J., Mose, M., de Paoli, F. V., Billeskov, T. B., Fred, R. G.,
1144 Pers, T. H., Pedersen, S. B., Petersen, K. K., Bjerre, M., Farup, J., & Jessen, N.
1145 (2021). Isolation and characterization of muscle stem cells, fibro-adipogenic
1146 progenitors, and macrophages from human skeletal muscle biopsies. *American*
1147 *Journal of Physiology-Cell Physiology*, *321*(2), C257–C268.
1148 https://doi.org/10.1152/ajpcell.00127.2021
1149 Ji, Y., Li, M., Chang, M., Liu, R., Qiu, J., Wang, K., Deng, C., Shen, Y., Zhu, J., Wang, W.,
1150 Xu, L., & Sun, H. (2022). Inflammation: Roles in Skeletal Muscle Atrophy.
1151 *Antioxidants (Basel, Switzerland)*, *11*(9), 1686.
1152 https://doi.org/10.3390/antiox11091686
1153 Judge, S. M., Nosacka, R. L., Delitto, D., Gerber, M. H., Cameron, M. E., Trevino, J. G., &
1154 Judge, A. R. (2018). Skeletal Muscle Fibrosis in Pancreatic Cancer Patients with
1155 Respect to Survival. *JNCI Cancer Spectrum*, *2*(3), pky043.
1156 https://doi.org/10.1093/jncics/pky043

Kajabadi, N., Low, M., Jacques, E., Lad, H., Tung, L. W., Babaeijandaghi, F., Gamu, D., Zelada, D., Wong, C. K., Chang, C., Yi, L., Wosczyna, M. N., Rando, T. A., Henríquez, J. P., Gibson, W. T., Gilbert, P. M., & Rossi, F. M. V. (2023). Activation of β-catenin in mesenchymal progenitors leads to muscle mass loss. *Developmental Cell*, *58*(6), 489-505.e7. https://doi.org/10.1016/j.devcel.2023.02.009

Kaneshige, A., Kaji, T., Zhang, L., Saito, H., Nakamura, A., Kurosawa, T., Ikemoto-Uezumi, M., Tsujikawa, K., Seno, S., Hori, M., Saito, Y., Matozaki, T., Maehara, K., Ohkawa, Y., Potente, M., Watanabe, S., Braun, T., Uezumi, A., & Fukada, S.-I. (2022). Relayed signaling between mesenchymal progenitors and muscle stem cells ensures adaptive stem cell response to increased mechanical load. *Cell Stem Cell*, *29*(2), 265-280.e6. https://doi.org/10.1016/j.stem.2021.11.003

Kimura, M., Naito, T., Kenmotsu, H., Taira, T., Wakuda, K., Oyakawa, T., Hisamatsu, Y., Tokito, T., Imai, H., Akamatsu, H., Ono, A., Kaira, K., Murakami, H., Endo, M., Mori, K., Takahashi, T., & Yamamoto, N. (2015). Prognostic impact of cancer cachexia in patients with advanced non-small cell lung cancer. *Supportive Care in Cancer*, *23*(6), 1699–1708. https://doi.org/10.1007/s00520-014-2534-3

Kunz, H. E., Port, J. D., Kaufman, K. R., Jatoi, A., Hart, C. R., Gries, K. J., Lanza, I. R., & Kumar, R. (2022). Skeletal muscle mitochondrial dysfunction and muscle and whole body functional deficits in cancer patients with weight loss. *Journal of Applied Physiology*, *132*(2), 388–401. https://doi.org/10.1152/japplphysiol.00746.2021

Kuswanto, W., Burzyn, D., Panduro, M., Wang, K. K., Jang, Y. C., Wagers, A. J., Benoist, C., & Mathis, D. (2016). Poor Repair of Skeletal Muscle in Aging Mice Reflects a

Defect in Local, Interleukin-33-Dependent Accumulation of Regulatory T Cells. *Immunity*, *44*(2), 355–367. https://doi.org/10.1016/j.immuni.2016.01.009

Lemos, D. R., Babaeijandaghi, F., Low, M., Chang, C.-K., Lee, S. T., Fiore, D., Zhang, R.-H., Natarajan, A., Nedospasov, S. A., & Rossi, F. M. V. (2015). Nilotinib reduces muscle fibrosis in chronic muscle injury by promoting TNF-mediated apoptosis of fibro/adipogenic progenitors. *Nature Medicine*, *21*(7), 786–794. https://doi.org/10.1038/nm.3869

Lin, T.-Y., Chen, Y.-F., Wu, W.-T., Han, D.-S., Tsai, I.-C., Chang, K.-V., & Özçakar, L. (2022). Impact of sarcopenia on the prognosis and treatment of lung cancer: An umbrella review. *Discover Oncology*, *13*(1), 115. https://doi.org/10.1007/s12672-022-00576-0

López-Armada, M. J., Riveiro-Naveira, R. R., Vaamonde-García, C., & Valcárcel-Ares, M. N. (2013). Mitochondrial dysfunction and the inflammatory response. *Mitochondrion*, *13*(2), 106–118. https://doi.org/10.1016/j.mito.2013.01.003

Loumaye, A., de Barsy, M., Nachit, M., Lause, P., Frateur, L., van Maanen, A., Trefois, P., Gruson, D., & Thissen, J.-P. (2015). Role of Activin A and Myostatin in Human Cancer Cachexia. *The Journal of Clinical Endocrinology & Metabolism*, *100*(5), 2030–2038. https://doi.org/10.1210/jc.2014-4318

Lukjanenko, L., Karaz, S., Stuelsatz, P., Gurriaran-Rodriguez, U., Michaud, J., Dammone, G., Sizzano, F., Mashinchian, O., Ancel, S., Migliavacca, E., Liot, S., Jacot, G., Metairon, S., Raymond, F., Descombes, P., Palini, A., Chazaud, B., Rudnicki, M. A., Bentzinger, C. F., & Feige, J. N. (2019). Aging Disrupts Muscle Stem Cell Function by Impairing Matricellular WISP1 Secretion from Fibro-

Adipogenic Progenitors. *Cell Stem Cell*, *24*(3), 433-446.e7. https://doi.org/10.1016/j.stem.2018.12.014

Madaro, L., Passafaro, M., Sala, D., Etxaniz, U., Lugarini, F., Proietti, D., Alfonsi, M. V., Nicoletti, C., Gatto, S., De Bardi, M., Rojas-García, R., Giordani, L., Marinelli, S., Pagliarini, V., Sette, C., Sacco, A., & Puri, P. L. (2018). Denervation-activated STAT3-IL6 signaling in fibro-adipogenic progenitors promotes myofibers atrophy and fibrosis. *Nature Cell Biology*, *20*(8), 917–927. https://doi.org/10.1038/s41556-018-0151-y

Mann, C. J., Perdiguero, E., Kharraz, Y., Aguilar, S., Pessina, P., Serrano, A. L., & Muñoz-Cánoves, P. (2011). Aberrant repair and fibrosis development in skeletal muscle. *Skeletal Muscle*, *1*(1), 21. https://doi.org/10.1186/2044-5040-1-21

Manoharan, R. R., Prasad, A., Pospíšil, P., & Kzhyshkowska, J. (2024). ROS signaling in innate immunity via oxidative protein modifications. *Frontiers in Immunology*, *15*. https://doi.org/10.3389/fimmu.2024.1359600

Marchi, S., Guilbaud, E., Tait, S. W. G., Yamazaki, T., & Galluzzi, L. (2023). Mitochondrial control of inflammation. *Nature Reviews Immunology*, *23*(3), 159–173. https://doi.org/10.1038/s41577-022-00760-x

Martin, L., Birdsell, L., MacDonald, N., Reiman, T., Clandinin, M. T., McCargar, L. J., Murphy, R., Ghosh, S., Sawyer, M. B., & Baracos, V. E. (2013). Cancer Cachexia in the Age of Obesity: Skeletal Muscle Depletion Is a Powerful Prognostic Factor, Independent of Body Mass Index. *Journal of Clinical Oncology*, *31*(12), 1539–1547. https://doi.org/10.1200/JCO.2012.45.2722

Mitchell, K. J., Pannérec, A., Cadot, B., Parlakian, A., Besson, V., Gomes, E. R., Marazzi, G., & Sassoon, D. A. (2010). Identification and characterization of a non-satellite

cell muscle resident progenitor during postnatal development. *Nature Cell Biology*, *12*(3), 257–266. https://doi.org/10.1038/ncb2025

Mohammed, F., Gorla, M., Bisoyi, V., Tammineni, P., & Sepuri, N. B. V. (2020). Rotenone-induced reactive oxygen species signal the recruitment of STAT3 to mitochondria. *FEBS Letters*, *594*(9), 1403–1412. https://doi.org/10.1002/1873-3468.13741

Neurohr, G. E., Terry, R. L., Lengefeld, J., Bonney, M., Brittingham, G. P., Moretto, F., Miettinen, T. P., Vaites, L. P., Soares, L. M., Paulo, J. A., Harper, J. W., Buratowski, S., Manalis, S., van Werven, F. J., Holt, L. J., & Amon, A. (2019). Excessive Cell Growth Causes Cytoplasm Dilution And Contributes to Senescence. *Cell*, *176*(5), 1083-1097.e18. https://doi.org/10.1016/j.cell.2019.01.018

Nordberg, J., & Arnér, E. S. (2001). Reactive oxygen species, antioxidants, and the mammalian thioredoxin system. *Free Radical Biology & Medicine*, *31*(11), 1287–1312. https://doi.org/10.1016/s0891-5849(01)00724-9

Nowaczyk, M., Malcher, A., Zimna, A., Łabędź, W., Kubaszewski, Ł., Fiedorowicz, K., Wierzbiński, K., Rozwadowska, N., & Kurpisz, M. (2020). Transient and Stable Overexpression of Extracellular Superoxide Dismutase is Positively Associated with the Myogenic Function of Human Skeletal Muscle-Derived Stem/Progenitor Cells. *Antioxidants*, *9*(9), Article 9. https://doi.org/10.3390/antiox9090817

Ørtenblad, N., Nielsen, J., Saltin, B., & Holmberg, H.-C. (2011). Role of glycogen availability in sarcoplasmic reticulum Ca2+ kinetics in human skeletal muscle. *The Journal of Physiology*, *589*(Pt 3), 711–725. https://doi.org/10.1113/jphysiol.2010.195982

Panci, G., & Chazaud, B. (2021). Inflammation during post-injury skeletal muscle regeneration. *Seminars in Cell & Developmental Biology*, *119*, 32–38. https://doi.org/10.1016/j.semcdb.2021.05.031

Qaisar, R., Pharaoh, G., Bhaskaran, S., Xu, H., Ranjit, R., Bian, J., Ahn, B., Georgescu, C., Wren, J. D., & Van Remmen, H. (2021). Restoration of Sarcoplasmic Reticulum Ca2+ ATPase (SERCA) Activity Prevents Age-Related Muscle Atrophy and Weakness in Mice. *International Journal of Molecular Sciences*, *22*(1), Article 1. https://doi.org/10.3390/ijms22010037

Riley, J. S., & Tait, S. W. (2020). Mitochondrial DNA in inflammation and immunity. *EMBO Reports*, *21*(4), e49799. https://doi.org/10.15252/embr.201949799

Roberts, B. M., Frye, G. S., Ahn, B., Ferreira, L. F., & Judge, A. R. (2013). Cancer cachexia decreases specific force and accelerates fatigue in limb muscle. *Biochemical and Biophysical Research Communications*, *435*(3), 488–492. https://doi.org/10.1016/j.bbrc.2013.05.018

Rodríguez, C., Timóteo-Ferreira, F., Minchiotti, G., Brunelli, S., & Guardiola, O. (2024). Cellular interactions and microenvironment dynamics in skeletal muscle regeneration and disease. *Frontiers in Cell and Developmental Biology*, *12*. https://doi.org/10.3389/fcell.2024.1385399

Rodríguez-Nuevo, A., Díaz-Ramos, A., Noguera, E., Díaz-Sáez, F., Duran, X., Muñoz, J. P., Romero, M., Plana, N., Sebastián, D., Tezze, C., Romanello, V., Ribas, F., Seco, J., Planet, E., Doctrow, S. R., González, J., Borràs, M., Liesa, M., Palacín, M., ... Zorzano, A. (2018). Mitochondrial DNA and TLR9 drive muscle inflammation upon Opa1 deficiency. *The EMBO Journal*, *37*(10), e96553. https://doi.org/10.15252/embj.201796553

Schindelin, J., Arganda-Carreras, I., Frise, E., Kaynig, V., Longair, M., Pietzsch, T., Preibisch, S., Rueden, C., Saalfeld, S., Schmid, B., Tinevez, J.-Y., White, D. J., Hartenstein, V., Eliceiri, K., Tomancak, P., & Cardona, A. (2012). Fiji: An open-source platform for biological-image analysis. *Nature Methods*, *9*(7), 676–682. https://doi.org/10.1038/nmeth.2019

Shoshan-Barmatz, V., & Ben-Hail, D. (2012). VDAC, a multi-functional mitochondrial protein as a pharmacological target. *Mitochondrion*, *12*(1), 24–34. https://doi.org/10.1016/j.mito.2011.04.001

Shoshan-Barmatz, V., & De, S. (2017). Mitochondrial VDAC, the Na+/Ca2+ Exchanger, and the Ca2+ Uniporter in Ca2+ Dynamics and Signaling. *Advances in Experimental Medicine and Biology*, *981*, 323–347. https://doi.org/10.1007/978-3-319-55858-5_13

Sliter, D. A., Martinez, J., Hao, L., Chen, X., Sun, N., Fischer, T. D., Burman, J. L., Li, Y., Zhang, Z., Narendra, D. P., Cai, H., Borsche, M., Klein, C., & Youle, R. J. (2018). Parkin and PINK1 mitigate STING-induced inflammation. *Nature*, *561*(7722), 258–262. https://doi.org/10.1038/s41586-018-0448-9

Smith, J. A. B., Murach, K. A., Dyar, K. A., & Zierath, J. R. (2023). Exercise metabolism and adaptation in skeletal muscle. *Nature Reviews Molecular Cell Biology*, *24*(9), 607–632. https://doi.org/10.1038/s41580-023-00606-x

Snoke, D. B., Bellefleur, E., Rehman, H. T., Carson, J. A., Poynter, M. E., Dittus, K. L., & Toth, M. J. (2023). Skeletal muscle adaptations in patients with lung cancer: Longitudinal observations from the whole body to cellular level. *Journal of Cachexia, Sarcopenia and Muscle*, *14*(6), 2579–2590. https://doi.org/10.1002/jcsm.13332

1300 Stephens, N. A., Skipworth, R. J. E., MacDonald, A. J., Greig, C. A., Ross, J. A., & Fearon,
1301 K. C. H. (2011). Intramyocellular lipid droplets increase with progression of
1302 cachexia in cancer patients. *Journal of Cachexia, Sarcopenia and Muscle*, *2*(2),
1303 111–117. https://doi.org/10.1007/s13539-011-0030-x
1304 Sullivan-Gunn, M. J., & Lewandowski, P. A. (2013). Elevated hydrogen peroxide and
1305 decreased catalase and glutathione peroxidase protection are associated with
1306 aging sarcopenia. *BMC Geriatrics*, *13*(1), 104. https://doi.org/10.1186/1471-
1307 2318-13-104
1308 Tang, H., Kim, M., Lee, M., Baumann, K., Olguin, F., He, H., Wang, Y., Jiang, B., Fang, S.,
1309 Zhu, J., Wang, K., Xia, H., Gao, Y., Konsker, H. B., Fatodu, E. A., Quarta, M.,
1310 Blonigan, J., Rando, T. A., & Shrager, J. B. (2022). Overexpression of thioredoxin-2
1311 attenuates age-related muscle loss by suppressing mitochondrial oxidative
1312 stress and apoptosis. *JCSM Rapid Communications*, *5*(1), 130–145.
1313 https://doi.org/10.1002/rco2.57
1314 Theret, M., Low, M., Rempel, L., Li, F. F., Tung, L. W., Contreras, O., Chang, C.-K., Wu,
1315 A., Soliman, H., & Rossi, F. M. (2021). Targeting fibrosis in the Duchenne
1316 Muscular Dystrophy mice model: An uphill battle. *bioRxiv*, 2021–01.
1317 Toth, M. J., Callahan, D. M., Miller, M. S., Tourville, T. W., Hackett, S. B., Couch, M. E., &
1318 Dittus, K. (2016). Skeletal muscle fiber size and fiber type distribution in human
1319 cancer: Effects of weight loss and relationship to physical function. *Clinical*
1320 *Nutrition*, *35*(6), 1359–1365. https://doi.org/10.1016/j.clnu.2016.02.016
1321 Uezumi, A., Ikemoto-Uezumi, M., Zhou, H., Kurosawa, T., Yoshimoto, Y., Nakatani, M.,
1322 Hitachi, K., Yamaguchi, H., Wakatsuki, S., Araki, T., Morita, M., Yamada, H.,
1323 Toyoda, M., Kanazawa, N., Nakazawa, T., Hino, J., Fukada, S.-I., & Tsuchida, K.

(2021). Mesenchymal Bmp3b expression maintains skeletal muscle integrity and decreases in age-related sarcopenia. *The Journal of Clinical Investigation*, *131*(1), e139617, 139617. https://doi.org/10.1172/JCI139617

VanderVeen, B. N., Murphy, E. A., & Carson, J. A. (2020). The Impact of Immune Cells on the Skeletal Muscle Microenvironment During Cancer Cachexia. *Frontiers in Physiology*, *11*. https://doi.org/10.3389/fphys.2020.01037

Vernochet, C., Mourier, A., Bezy, O., Macotela, Y., Boucher, J., Rardin, M. J., An, D., Lee, K. Y., Ilkayeva, O. R., Zingaretti, C. M., Emanuelli, B., Smyth, G., Cinti, S., Newgard, C. B., Gibson, B. W., Larsson, N.-G., & Kahn, C. R. (2012). Adipose-Specific Deletion of TFAM Increases Mitochondrial Oxidation and Protects Mice against Obesity and Insulin Resistance. *Cell Metabolism*, *16*(6), 765–776. https://doi.org/10.1016/j.cmet.2012.10.016

Vidal, B., Serrano, A. L., Tjwa, M., Suelves, M., Ardite, E., Mori, R. D., Baeza-Raja, B., Lagrán, M. M. de, Lafuste, P., Ruiz-Bonilla, V., Jardí, M., Gherardi, R., Christov, C., Dierssen, M., Carmeliet, P., Degen, J. L., Dewerchin, M., & Muñoz-Cánoves, P. (2008). Fibrinogen drives dystrophic muscle fibrosis via a TGFβ/alternative macrophage activation pathway. *Genes & Development*, *22*(13), 1747. https://doi.org/10.1101/gad.465908

Washington, T. A., Schrems, E. R., Haynie, W. S., Rosa-Caldwell, M. E., Brown, J. L., Saling, L., Lim, S., Perry Jr., R. A., Brown, L. A., Lee, D. E., & Greene, N. P. (2023). Development of skeletal muscle fibrosis in a rodent model of cancer cachexia. *Cell Biochemistry and Function*, *41*(4), 478–489. https://doi.org/10.1002/cbf.3797

West, A. P., Khoury-Hanold, W., Staron, M., Tal, M. C., Pineda, C. M., Lang, S. M., Bestwick, M., Duguay, B. A., Raimundo, N., MacDuff, D. A., Kaech, S. M., Smiley, J. R., Means, R. E., Iwasaki, A., & Shadel, G. S. (2015). Mitochondrial DNA stress primes the antiviral innate immune response. *Nature*, *520*(7548), 553–557. https://doi.org/10.1038/nature14156

Wosczyna, M. N., Konishi, C. T., Perez Carbajal, E. E., Wang, T. T., Walsh, R. A., Gan, Q., Wagner, M. W., & Rando, T. A. (2019). Mesenchymal Stromal Cells Are Required for Regeneration and Homeostatic Maintenance of Skeletal Muscle. *Cell Reports*, *27*(7), 2029-2035.e5. https://doi.org/10.1016/j.celrep.2019.04.074

Xiang, Y., Dai, J., Li, Y., You, Z., Zhang, J., Huang, X., Nie, S., Chen, Y., Xu, L., Liu, F., Jiang, J., & Xu, J. (2022). ROS-activated CXCR2+ neutrophils recruited by CXCL1 delay denervated skeletal muscle atrophy and undergo P53-mediated apoptosis. *Experimental & Molecular Medicine*, *54*(7), 1011–1023. https://doi.org/10.1038/s12276-022-00805-0

Xu, Z., Fu, T., Guo, Q., Zhou, D., Sun, W., Zhou, Z., Chen, X., Zhang, J., Liu, L., Xiao, L., Yin, Y., Jia, Y., Pang, E., Chen, Y., Pan, X., Fang, L., Zhu, M., Fei, W., Lu, B., & Gan, Z. (2022). Disuse-associated loss of the protease LONP1 in muscle impairs mitochondrial function and causes reduced skeletal muscle mass and strength. *Nature Communications*, *13*(1), 894. https://doi.org/10.1038/s41467-022-28557-5

Yao, Y., Luo, Y., Liang, X., Zhong, L., Wang, Y., Hong, Z., Song, C., Xu, Z., Wang, J., & Zhang, M. (2025). The role of oxidative stress-mediated fibro-adipogenic progenitor senescence in skeletal muscle regeneration and repair. *Stem Cell Research & Therapy*, *16*(1), 104. https://doi.org/10.1186/s13287-025-04242-4

Yu, X., Chen, X., Su, Y., Tang, H., & Xie, L. (2024). Causal role of immune cells in muscle atrophy: Mendelian randomization study. *Scientific Reports*, *14*(1), 25878. https://doi.org/10.1038/s41598-024-76828-6

Zelko, I. N., Mariani, T. J., & Folz, R. J. (2002). Superoxide dismutase multigene family: A comparison of the CuZn-SOD (SOD1), Mn-SOD (SOD2), and EC-SOD (SOD3) gene structures, evolution, and expression. *Free Radical Biology & Medicine*, *33*(3), 337–349. https://doi.org/10.1016/s0891-5849(02)00905-x

Zhang, W., Liu, Y., & Zhang, H. (2021). Extracellular matrix: An important regulator of cell functions and skeletal muscle development. *Cell & Bioscience*, *11*(1), 65. https://doi.org/10.1186/s13578-021-00579-4

Zhang, Y., Xia, M., Zhao, T., Zhang, Q., Li, R., & Yang, L. (2023). Camk2a suppresses denervated muscle atrophy by maintaining the Ca2+ homeostasis in muscle cells. *Cellular and Molecular Biology (Noisy-Le-Grand, France)*, *69*(11), 25–29. https://doi.org/10.14715/cmb/2023.69.11.4

Zhang, Z., Sliter, D. A., Bleck, C. K. E., & Ding, S. (2019). Fis1 deficiencies differentially affect mitochondrial quality in skeletal muscle. *Mitochondrion*, *49*, 217–226. https://doi.org/10.1016/j.mito.2019.09.005

Tables

Table 1

Variable	Patients	Controls
Sex	N=18	N=18
Male	N=9	N=9
Female	N=9	N=9
Age	N=18	N=18
Mean (SD)	64.2 (10.5)	64.8 (7.5)
Min-Max	46-80	54-79
BMI		
Mean (SD)	24.9 (5.6)	25.2 (5.8)
Min-Max	16-41	20-45
BMI (kg/m^2) < 20 N(%)	3 (16.7)	0 (0)
Cachexia status at diagnosis		
Cachectic N(%)	8(44.4)	0 (0)
Pre-cachectic N(%)	4 (22.2)	0 (0)
Non-cachectic N(%)	6 (33.3)	0 (0)

Table 1. Study participant characteristics.

Figure legends

Figure 1. Skeletal muscle microenvironment structural and proteomic remodelling in patients with NSCLC. (**a**) Representative cryosections of skeletal muscle tissue from controls and patients with NSCLC: Laminin (magenta), type I (blue) and type II (green) muscle fibers. (**b**) Quantification of fiber cross-sectional area (CSA, μm^2) in type I and type II fibers. Data points represent the mean fiber CSA for each participant. (**c**) Frequency distribution of muscle fiber CSA in type I fibers and (**d**) percentage of type I fibers < 4000 μm^2. (**e**) Frequency distribution of type II fibers and (**f**) percentage of type II fibers < 2000 μm^2. (**g-k**) Representative images of BODIPY (green) and Laminin (magenta) staining and quantifications of lipid deposition in the ECM (% fibers) and ECM/cytosolic lipid intensity ratio, BODIPY intensity (arbitrary units, AU), lipid droplet area (μm^2). (**l-m**) Representative images and quantification (% area) of picosirius red staining. (**n**) Volcano plot showing Log2 Fold change (Log2FC) and –log10 p values of proteins analyzed by proteomics. (**o-p**) Gene ontology terms related to histological findings; enrichment of proteins significantly upregulated (**o**) and differentially regulated (**p**) in patients with NSCLC vs controls. (**q-s**) Log2FC of proteins upregulated between NSCLC and controls. (**b**) Two-way ANOVA. (**d, f, h-k, m**) Student's T-test. (**q-s**) Welch's T-test. ME: main effect (**a**, **g**, **l**) Scale bar 100 µm.

Figure 2. Greater predominance of CD90- FAPs and increased MuSC size in patients with NSCLC. (**a**) CD90- FAP (CD34+; CD31-; CD45-) proportion (%) and (**b**) CD90- FAP size (FSC-W). (**c**) Total FAP content (cells per mg of tissue) and (**d**) size (FSC-W). (**e**) Representative images of FAPs stained with DAPI (blue), EdU (incorporated into newly synthesized DNA, red) and (**f**) quantification of EdU incorporation (%) over 5 days in culture. (**g**) Representative images and (**h**) quantification of myotube diameter in C2C12 myotubes treated with conditioned media from FAPs derived from patients and controls (**i**) Muscle stem cell (MuSC, CD82+; CD56+; CD45-; CD31-; CD34-) content (cells per mg of tissue) and (**j**) MuSC size (FSC-W) in patients with NSCLC and controls. (**k**) Representative images of MuSCs stained with DAPI (blue), EdU (incorporated into newly synthesized DNA, green) and (**l**) quantification of EdU incorporation (%) (over 3 days in culture). (**a-d, f, h-j, l**) Student's T-test. (**e**, **g**, **k**) Scale bar 275 µm.

Figure 3. NSCLC skeletal muscle exhibits mitochondrial alterations. (**a**) Over-representation analysis showing enrichment of mitochondrial biological processes among differentially expressed proteins. (**b**) Log2 fold changes in mitochondrial protein abundance (COX8A, OXA1L, NNT, MRPL24) in NSCLC muscle compared to controls. (**c**) Mitochondrial respiratory capacity. (**d-f**) Band densitometry quantification of OxPhos subunit, TFAM and mitochondrial mass markers. (**g**) Representative immunofluorescence images of Type I and Type II muscle fibers, stained with a COXIV antibody to visualize mitochondrial network organization (cyan), Quantification of (**h**) mitochondrial fractional area (%) and (**i**) fragmentation index. (**b**) False discovery rate (FDR). (**c, d, f, h, i**) Two-way ANOVA. (**e**) Student's T-test. (**g)** Scale bar 5 µm.

Figure 4. Mitochondrial oxidative stress and calcium dysregulation in NSCLC skeletal muscle. (a) Enriched gene ontology terms related to mitochondrial redox and calcium ion transport in proteins differentially expressed in NSCLC vs controls. (**b**) Log2 fold (Log2FC) changes in mitochondrial protein abundance (TXN2, PRDX3, SOD3, CAT, CAMK2A, VDAC2, HRC) in NSCLC muscle compared to controls. (**c, e**) Band densitometry quantification of PRDX2 and PRDX3 monomers. (**d, f**) Dimer/monomer ratio quantification of PRDX2 and PRDX3. (**g**) Band densitometry quantification of VDAC1. (**h**) Sarcoplasmic reticulum calcium uptake rate (Tau, expressed as a reciprocal). (**i**) Sarcoplasmic uptake rate at 400 nM (high) and 200 nM (low) Ca2+ concentrations, release rate, and estimation of vesicle leak using Cyclopiazonic acid (CPA) (nmol/gr ww/min). (**j**) Band densitometry quantification of SERCA 1 and 2, STIM1 (stromal interaction molecule 1) and CSQ1 (calsequestrin 1). (**b**) False discovery rate (FDR). (**c-h**) Student's T-test. (**i, j**) Two-way ANOVA.

Figure 5. Enhanced inflammatory and immune response in patients with NSCLC. (a) Gene Ontology over-representation analysis showing enrichment of immune and inflammatory processes among proteins upregulated in NSCLC. (**b**) Log2 fold (Log2FC) changes in the abundance of proteins related to inflammatory response, acute-phase response, and cytokine production. Proteins include CRP, C3, HP, ORM1, S100A8, and others associated with inflammation. **(c-d)** CRP and GDF15 plasma levels. (**e-f**) Skeletal muscle *GDF-15* and inflammatory gene expression. **(g-h)** P65, STAT3 and pSTAT3 protein content. **(i)** Summary of gating strategy for immune cell subsets. **(j)** Overall hematopoetic cell (CD45+) content (cells per mg of tissue). **(k)** Macrophage (CD45+; CD14+ monocyte) content (cells per mg of tissue). **(l)** Pro-inflammatory macrophages/monocytes (CD11c+CD45+CD14+) content (cells per mg of tissue). **(m)** Anti-inflammatory macrophages/monocyte (CD11c-CD45+CD14+) content (cells per mg of tissue)**. (n)** Lymphocyte **(**CD45+; CD14- cell SSClow) content (cells per mg of tissue). Macrophage (**o**) and lymphocyte (**p**) to hematopoietic cell ratio. (**b**) False discovery rate (FDR). (**c-e, g, h, j-p**) Student's T-test. (**f**) Two-way ANOVA.

Figure 1

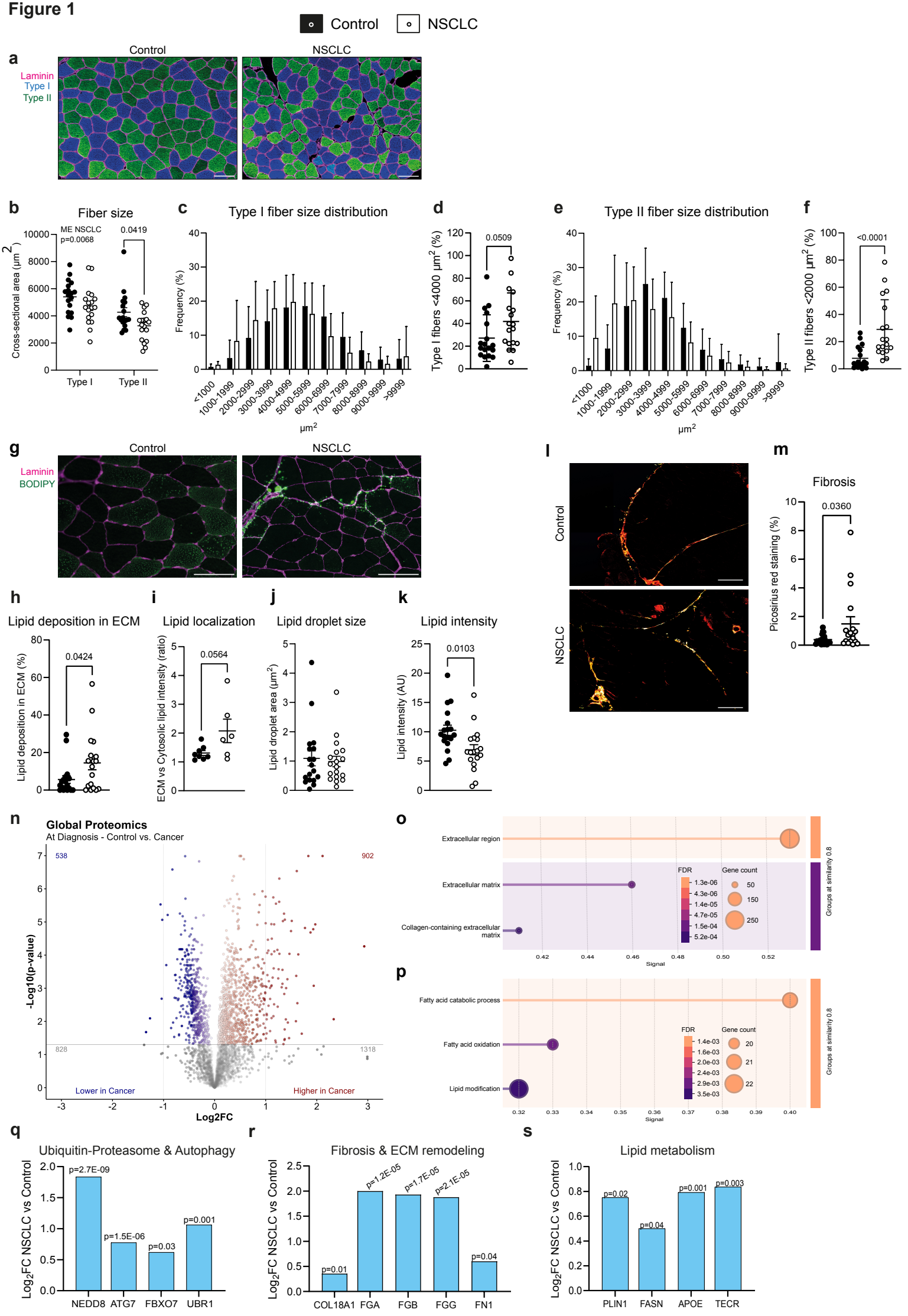
Control
NSCLC
a
Laminin
Type I
Type II
b
Fiber size
ME NSCLC
p=0.0068
0.0419
Cross-sectional area (µm2)
Type I
Type II
c
Type I fiber size distribution
Frequency (%)
<1000
1000-1999
2000-2999
3000-3999
4000-4999
5000-5999
6000-6999
7000-7999
8000-8999
9000-9999
>9999
µm2
d
0.0509
Type I fibers <4000 µm2 (%)
e
Type II fiber size distribution
f
<0.0001
Type II fibers <2000 µm2 (%)
g
BODIPY
h
Lipid deposition in ECM
0.0424
Lipid deposition in ECM (%)
i
Lipid localization
0.0564
ECM vs Cytosolic lipid intensity (ratio)
j
Lipid droplet size
Lipid droplet area (µm2)
k
Lipid intensity
0.0103
Lipid intensity (AU)
l
m
Fibrosis
0.0360
Picosirius red staining (%)
n
Global Proteomics
At Diagnosis - Control vs. Cancer
538
902
828
1318
Lower in Cancer
Higher in Cancer
-Log10(p-value)
Log2FC
o
Extracellular region
Extracellular matrix
Collagen-containing extracellular matrix
FDR
Gene count
Groups at similarity 0.8
Signal
p
Fatty acid catabolic process
Fatty acid oxidation
Lipid modification
q
Ubiquitin-Proteasome & Autophagy
Log2FC NSCLC vs Control
p=2.7E-09
p=1.5E-06
p=0.03
p=0.001
NEDD8
ATG7
FBXO7
UBR1
r
Fibrosis & ECM remodeling
p=0.01
p=1.2E-05
p=1.7E-05
p=2.1E-05
p=0.04
COL18A1
FGA
FGB
FGG
FN1
s
Lipid metabolism
p=0.02
p=0.04
p=0.001
p=0.003
PLIN1
FASN
APOE
TECR

Figure 2

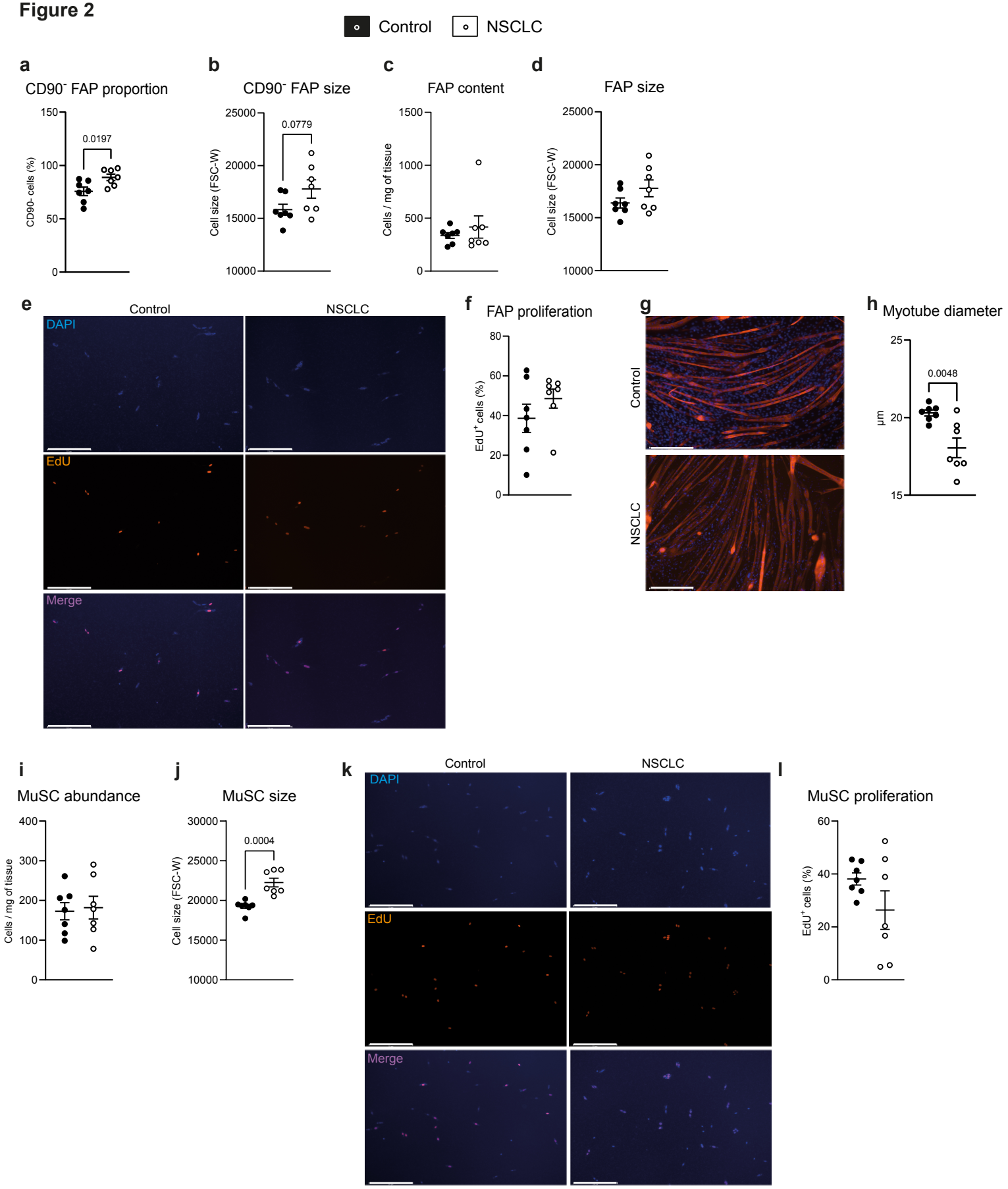
Control
NSCLC
a
CD90⁻ FAP proportion
CD90- cells (%)
0.0197
b
CD90⁻ FAP size
Cell size (FSC-W)
0.0779
c
FAP content
Cells / mg of tissue
d
FAP size
Cell size (FSC-W)
e
Control
NSCLC
DAPI
EdU
Merge
f
FAP proliferation
EdU⁺ cells (%)
g
Control
NSCLC
h
Myotube diameter
µm
0.0048
i
MuSC abundance
Cells / mg of tissue
j
MuSC size
Cell size (FSC-W)
0.0004
k
Control
NSCLC
DAPI
EdU
Merge
l
MuSC proliferation
EdU⁺ cells (%)

Figure 3

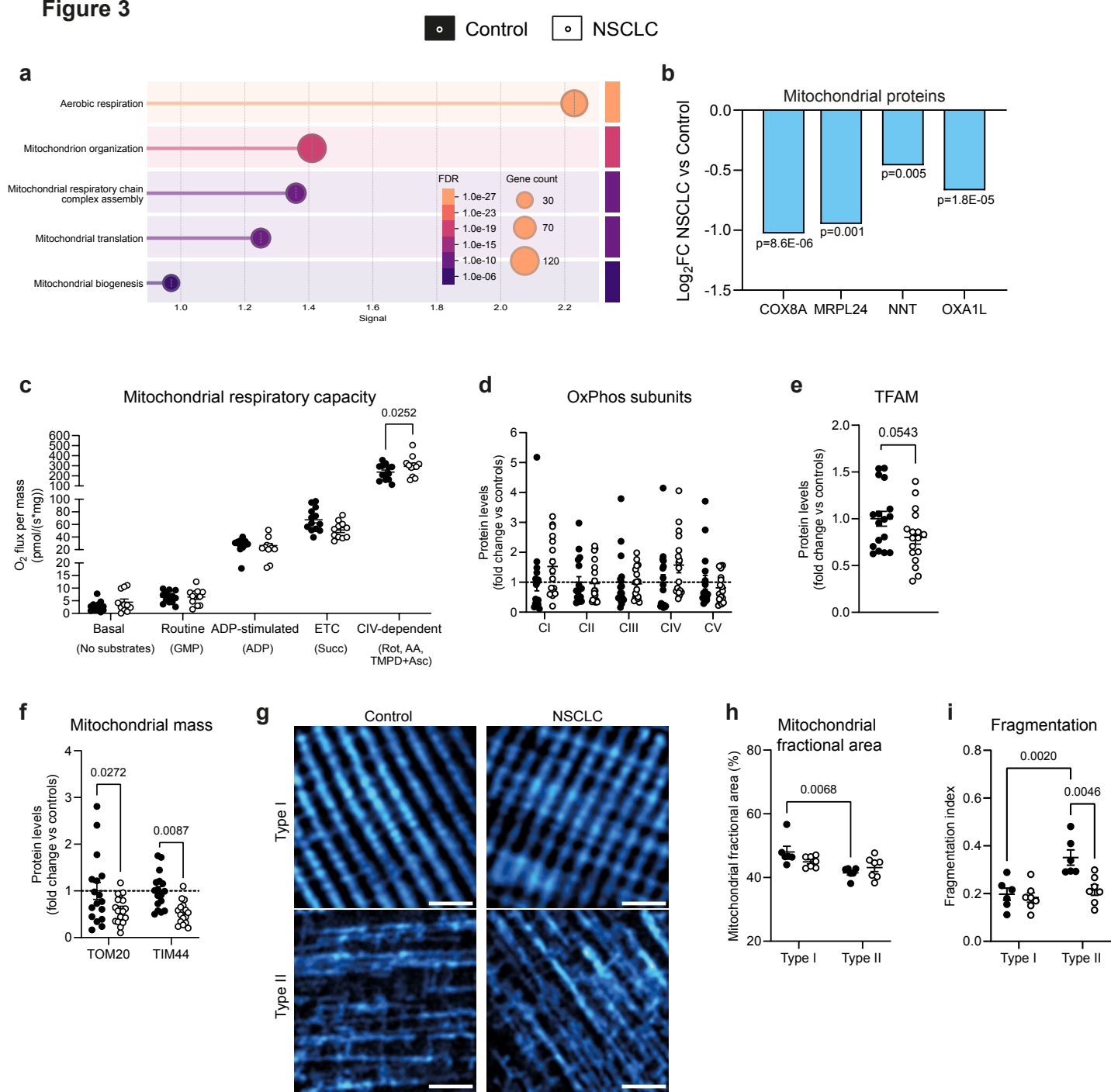
Control
NSCLC
a
Aerobic respiration
Mitochondrion organization
Mitochondrial respiratory chain complex assembly
Mitochondrial translation
Mitochondrial biogenesis
FDR
1.0e-27
1.0e-23
1.0e-19
1.0e-15
1.0e-10
1.0e-06
Gene count
30
70
120
1.0
1.2
1.4
1.6
1.8
2.0
2.2
Signal
b
Mitochondrial proteins
Log2FC NSCLC vs Control
0.0
-0.5
-1.0
-1.5
p=8.6E-06
p=0.001
p=0.005
p=1.8E-05
COX8A
MRPL24
NNT
OXA1L
c
Mitochondrial respiratory capacity
O2 flux per mass (pmol/(s*mg))
0.0252
Basal (No substrates)
Routine (GMP)
ADP-stimulated (ADP)
ETC (Succ)
CIV-dependent (Rot, AA, TMPD+Asc)
d
OxPhos subunits
Protein levels (fold change vs controls)
CI
CII
CIII
CIV
CV
e
TFAM
Protein levels (fold change vs controls)
0.0543
f
Mitochondrial mass
Protein levels (fold change vs controls)
0.0272
0.0087
TOM20
TIM44
g
Control
NSCLC
Type I
Type II
h
Mitochondrial fractional area
Mitochondrial fractional area (%)
0.0068
Type I
Type II
i
Fragmentation
Fragmentation index
0.0020
0.0046
Type I
Type II

Figure 4

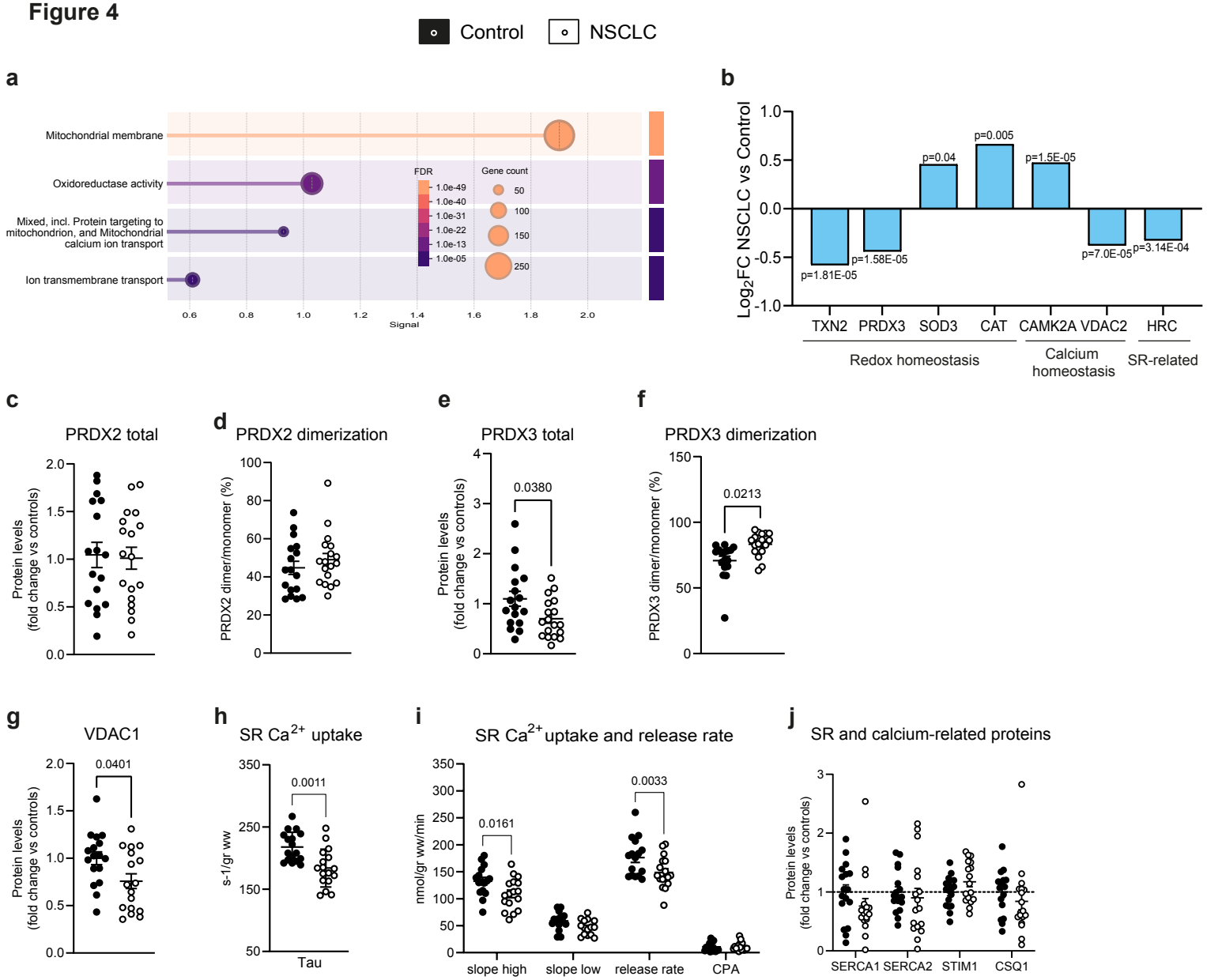
Control
NSCLC
a
Mitochondrial membrane
Oxidoreductase activity
Mixed, incl. Protein targeting to mitochondrion, and Mitochondrial calcium ion transport
Ion transmembrane transport
FDR
1.0e-49
1.0e-40
1.0e-31
1.0e-22
1.0e-13
1.0e-05
Gene count
50
100
150
250
0.6
0.8
1.0
1.2
1.4
1.6
1.8
2.0
Signal
b
Log2FC NSCLC vs Control
1.0
0.5
0.0
-0.5
-1.0
p=1.81E-05
p=1.58E-05
p=0.04
p=0.005
p=1.5E-05
p=7.0E-05
p=3.14E-04
TXN2
PRDX3
SOD3
CAT
CAMK2A
VDAC2
HRC
Redox homeostasis
Calcium homeostasis
SR-related
c
PRDX2 total
Protein levels (fold change vs controls)
d
PRDX2 dimerization
PRDX2 dimer/monomer (%)
e
PRDX3 total
0.0380
f
PRDX3 dimerization
PRDX3 dimer/monomer (%)
0.0213
g
VDAC1
0.0401
h
SR Ca2+ uptake
s-1/gr ww
0.0011
Tau
i
SR Ca2+ uptake and release rate
nmol/gr ww/min
0.0161
0.0033
slope high
slope low
release rate
CPA
j
SR and calcium-related proteins
SERCA1
SERCA2
STIM1
CSQ1

Figure 5

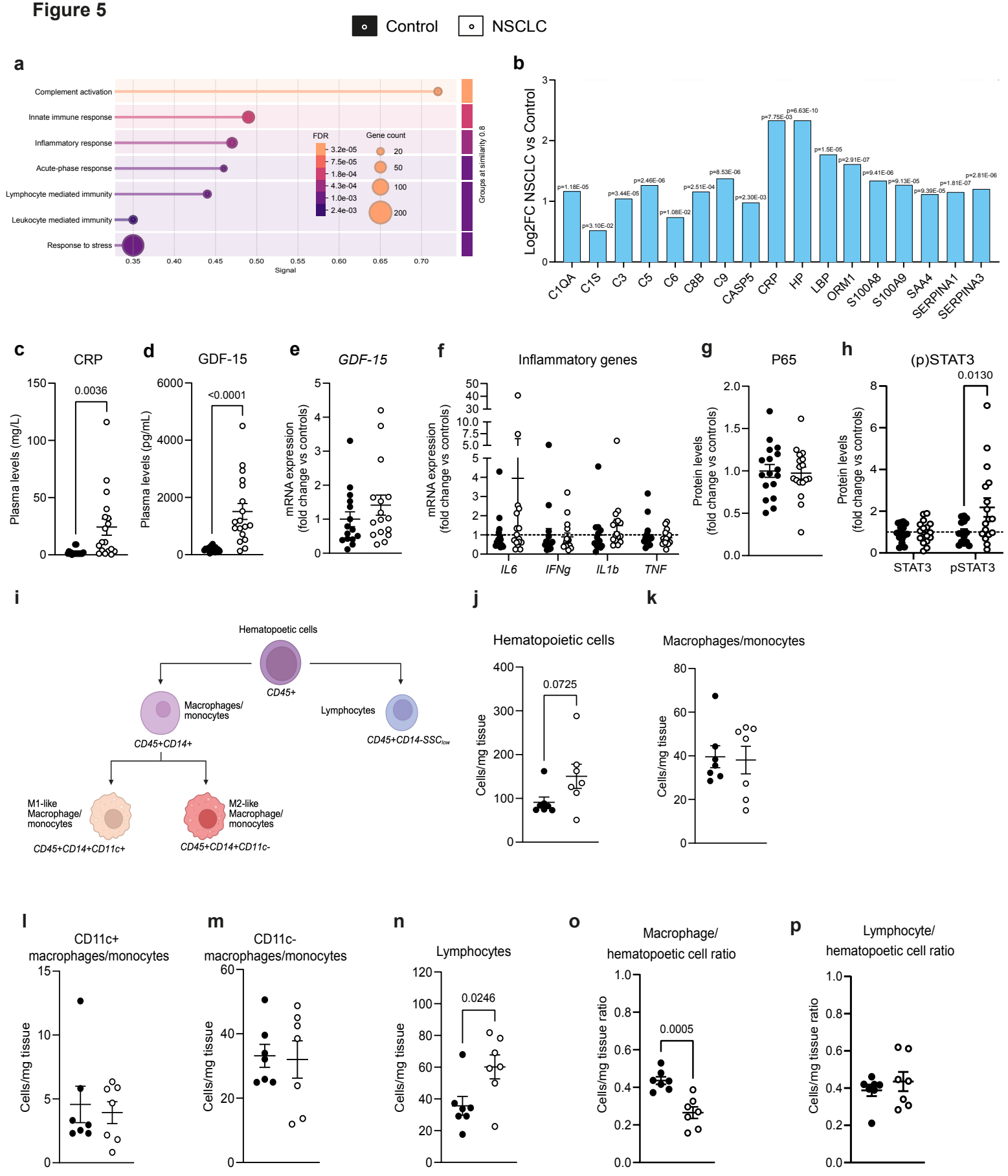
Control
NSCLC
a
Complement activation
Innate immune response
Inflammatory response
Acute-phase response
Lymphocyte mediated immunity
Leukocyte mediated immunity
Response to stress
FDR
3.2e-05
7.5e-05
1.8e-04
4.3e-04
1.0e-03
2.4e-03
Gene count
20
50
100
200
Groups at similarity 0.8
Signal
b
Log2FC NSCLC vs Control
C1QA
C1S
C3
C5
C6
C8B
C9
CASP5
CRP
HP
LBP
ORM1
S100A8
S100A9
SAA4
SERPINA1
SERPINA3
c
CRP
Plasma levels (mg/L)
0.0036
d
GDF-15
Plasma levels (pg/mL)
<0.0001
e
GDF-15
mRNA expression (fold change vs controls)
f
Inflammatory genes
mRNA expression (fold change vs controls)
IL6
IFNg
IL1b
TNF
g
P65
Protein levels (fold change vs controls)
h
(p)STAT3
Protein levels (fold change vs controls)
0.0130
STAT3
pSTAT3
i
Hematopoetic cells
CD45+
Macrophages/ monocytes
CD45+CD14+
Lymphocytes
CD45+CD14-SSC$_{low}$
M1-like Macrophage/ monocytes
CD45+CD14+CD11c+
M2-like Macrophage/ monocytes
CD45+CD14+CD11c-
j
Hematopoietic cells
Cells/mg tissue
0.0725
k
Macrophages/monocytes
Cells/mg tissue
l
CD11c+ macrophages/monocytes
Cells/mg tissue
m
CD11c- macrophages/monocytes
Cells/mg tissue
n
Lymphocytes
Cells/mg tissue
0.0246
o
Macrophage/ hematopoetic cell ratio
Cells/mg tissue ratio
0.0005
p
Lymphocyte/ hematopoetic cell ratio
Cells/mg tissue ratio

Supplementary Information

Pathophysiological remodelling of the skeletal muscle microenvironment in patients with lung cancer

Supplementary Table 1. SYBR green primer pairs used in gene expression analyses.

Targeted gene	*Forward sequence*	*Reverse sequence*	*Source*
GDF-15	GACCCTCAGAGTTGCACTCC	GCCTGGTTAGCAGGTCCTC	Primerbank
IL6	ACTCACCTCTTCAGAACGAATTG	CCATCTTTGGAAGGTTCAGGTTG	Primerbank
IFNg	TCGGTAACTGACTTGAATGTCCA	TCGCTTCCCTGTTTTAGCTGC	Primerbank
IL1b	TTCGACACATGGGATAACGAGG	TTTTTGCTGTGAGTCCCGGAG	Primerbank
TNF	CCTCTCTCTAATCAGCCCTCTG	GAGGACCTGGGAGTAGATGAG	Primerbank
mtND1	GAACACCTCTGATTACTC	GTATTCGGCTATGAAGAA	(Wangpermtam et al., 2019)
mtCO1	CAGTCTACCCTCCCTTAGCA	TGATGGCCCCTAAGATAGAG	(Wangpermtam et al., 2019)
mtAPTase6	ACACTAAAGGACGAACCTGA	GGTGGTTGGTGTAAATGAGT	(Wangpermtam et al., 2019)
PPARGC1a	TCTGAGTCTGTATGGAGTGACAT	CCAAGTCGTTCACATCTAGTTCA	Primerbank
RPLP0	AGCCCAGAACACTGGTCTC	ACTCAGGATTTCAATGGTGCC	Primerbank

Supplementary Table 2. Primary antibodies used in immunoblotting assays.

Targeted protein	*Catalog no.*	*Company*	*Dilution*
Anti-ATROGIN1	sc-166806	Santa Cruz Biotechnology	1:1000 in TBST
Anti-MuRF1	sc-398608	Santa Cruz Biotechnology	1:1000 in TBST
Anti-P62 (SQSTM1)	51143	Cell Signaling	1:1000 in 2% skim milk
Anti-OXPHOS cocktail	ab110411	Abcam	1:1000 in 3% BSA
Anti-TFAM	ab131607	Abcam	1:1000 in 3% BSA
Anti-TOM20	sc-17764	Santa Cruz Biotechnology	1:1000 in 2% skim milk
Anti-TIM44	sc-390755	Santa Cruz Biotechnology	1:1000 in 2% skim milk
Anti-VDAC1	sc-390996	Santa Cruz Biotechnology	1:1000 in 2% skim milk
Anti-MFN1	sc-166644	Santa Cruz Biotechnology	1:1000 in TBST
Anti-MFN2	119255	Cell Signalling	1:1000 in TBST
Anti-DPR1	sc-271583	Santa Cruz Biotechnology	1:1000 in TBST
Anti-PRDX2	ab109387	Abcam	1:1000 in 3% BSA
Anti-PRDX3	ab73349	Abcam	1:1000 in 3% BSA
Anti-SOD2	o6984	Milipore	1:1000 in 3% BSA
Anti-P65	sc-8008	Santa Cruz Biotechnology	1:1000 in 2% skim milk
Anti-STAT3	Sc-8019	Santa Cruz Biotechnology	1:1000 in 3% BSA
Anti-p-STAT3(Tyr705)	9138s	Cell Signalling	1:1000 in 3% BSA
Anti-SERCA1	MA3-912	Invitrogen	1:1000 in TBST
Anti-SERCA2	MA3-910	Invitrogen	1:1000 in 2% skim milk
Anti-STIM1	49163	Cell Signalling	1:1000 in TBST
Anti-CSQ1	PA1-193	Invitrogen	1:1000 in 2% skim milk
Anti-MHC (MF20)	MAB4470	R&D	1:25 in 1% BSA

TBST: tris-buffered saline with tween 20; BSA: bovine serum albumin.

Supplementary Table 3. Primary antibodies used in fluorescence-activated cell sorting analyses.

Targeted protein	*Catalog no.*	*Company*	*Volume per sample*
Anti-CD31-BUV395	700 130-110-673	Miltenyi Biotec	2 uL
Anti-CD90-PE	120909-42	Invitrogen	3.6 uL
Anti-CD14-BV605	564054	BD Biosciences	5 uL
Anti-CD11c-APCvio770	130-113-585	Miltenyi Biotec	5 uL
Anti-CD56-BV421	562751	BD Bioscience	5 uL
Anti-CD82-PE-Vio770	130-101-302	Miltenyi Biotec	10 uL
Anti-CD34-APC	666824	BD Bioscience	20 uL
Anti-CD45-VioBright FITC	130-114-567	Miltenyi Biotec	12 uL

Supplementary Figure 1. (**a**) Isolated single muscle fibers stained to visualize Actin (magenta). (**b**) Fiber type proportions. (**c**) Fiber type-specific BODIPY quantification. (**d**) BODIPY quantification ratio between fiber type I and II. (**e**) PAS staining of skeletal muscle sections. (**f**) Principal component analysis of global skeletal muscle proteomic profiles. (**g**) Representative immunoblots of ATROGIN1, MuRF1 and P62 and (**h, i**) band densitometry quantification. (**b, c, h**) Two-way ANOVA. (**d, i**) Student's T-test. (**c**) Scale bars 100 µm.

Supplementary Figure 2. Overview of in vitro experiments using FAPs isolated from controls and patients with NSCLC. Proliferative capacity was assessed by 5-ethynyl-2'-deoxyuridine (EdU) incorporation, and the effect of FAP-conditioned media on muscle size regulation was evaluated in C2C12 myotubes.

Supplementary Figure 3. (**a**) Enriched mitochondria-related terms identified by over-representation analysis of proteins downregulated in NSCLC compared with controls. (**b**) Representative immunoblot of OxPhos subunits. (**c**) mRNA expression of mitochondrial transcripts. (**d**) Representative immunoblot of TFAM. (**e**) mRNA expression of *PPARGC1a*. (**f**) Representative immunoblots of TOM20 and TIM44. (**g**) Representative immunoblots and band densitometry quantification of MFN1, MFN2 and DRP1. (**c, h**) Two-way ANOVA. (**e**) Student's T-test.

Supplementary Figure 4. (**a**) Schematic of expected band densitometry upon increasing intracellular H2O2 levels. (**b**) Representative immunoblot of PRDX2, PRDX3 and SOD2. (**c**) Band densitometry quantification of SOD2. (**d**) Muscle H2O2 levels. (**e**) Representative immunoblot of VDAC1, SERCA1, SERCA2, CSQ1, STIM1. (**c, d**) Student's T-test.

Supplementary Figure 5. (**a**) Representative immunoblot of P65, STAT3 and phosphorylated STAT3(Tyr705). (**b**) Gene expression levels of C3 in FAP subsets of patients with NSCLC. (**b**) Student's T-test.

Supplementary Figure 1

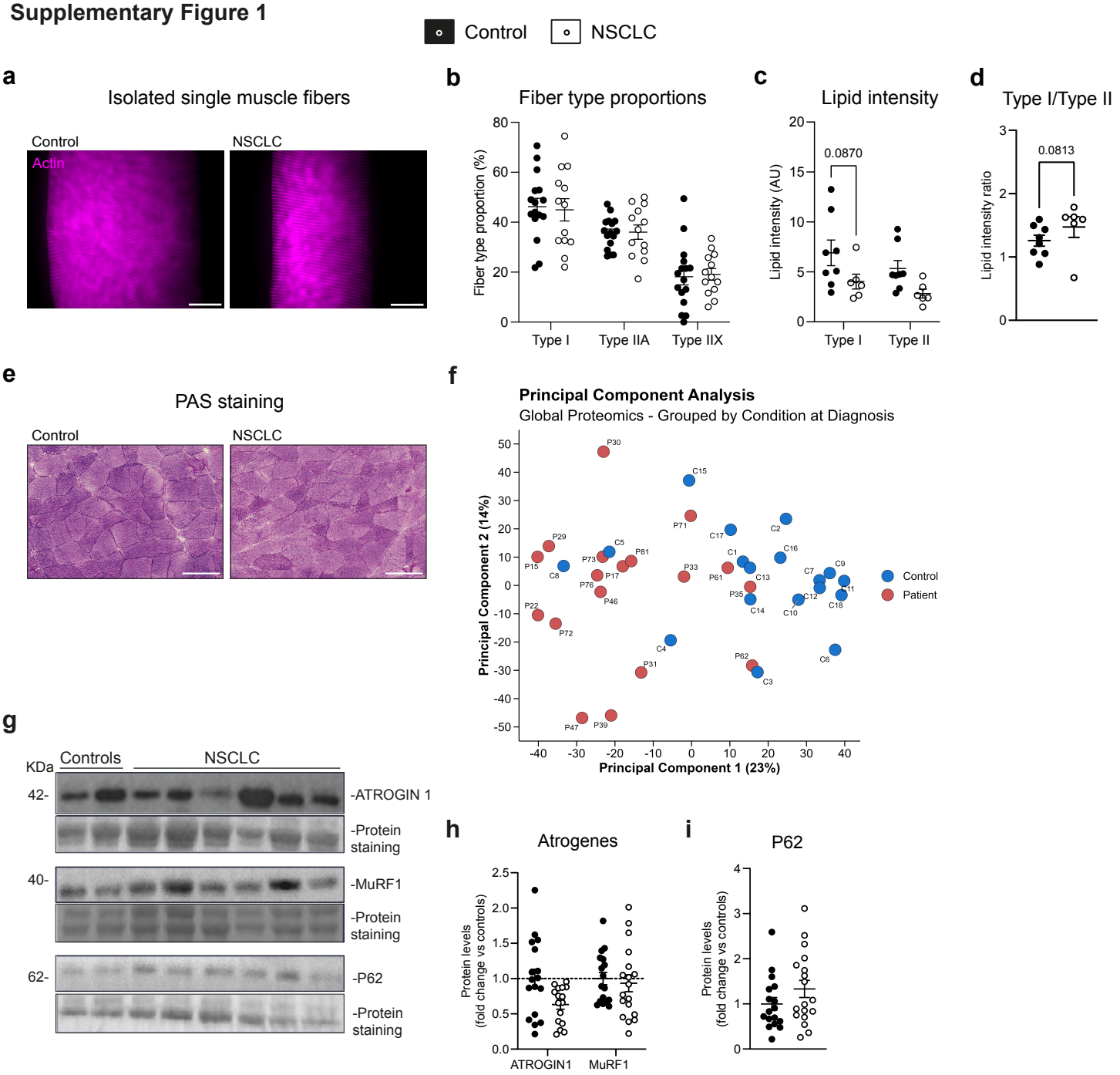

Supplementary Figure 2

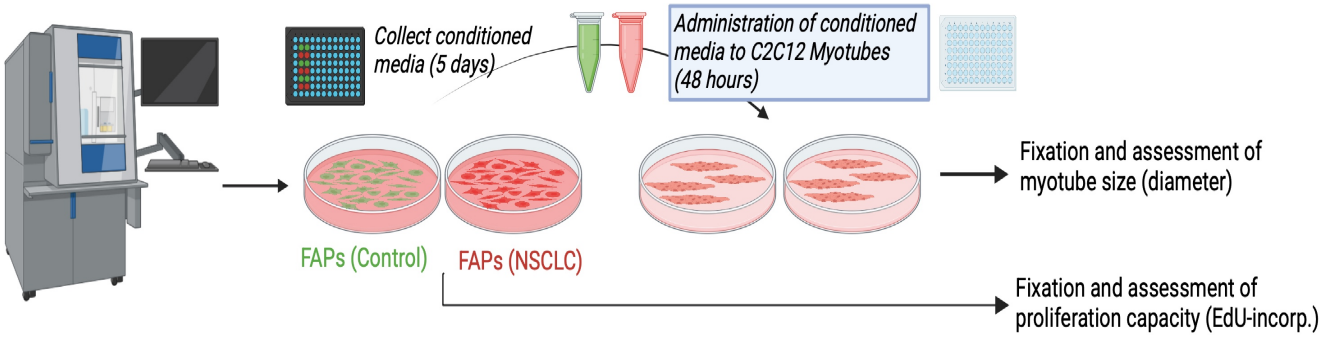

Supplementary Figure 3

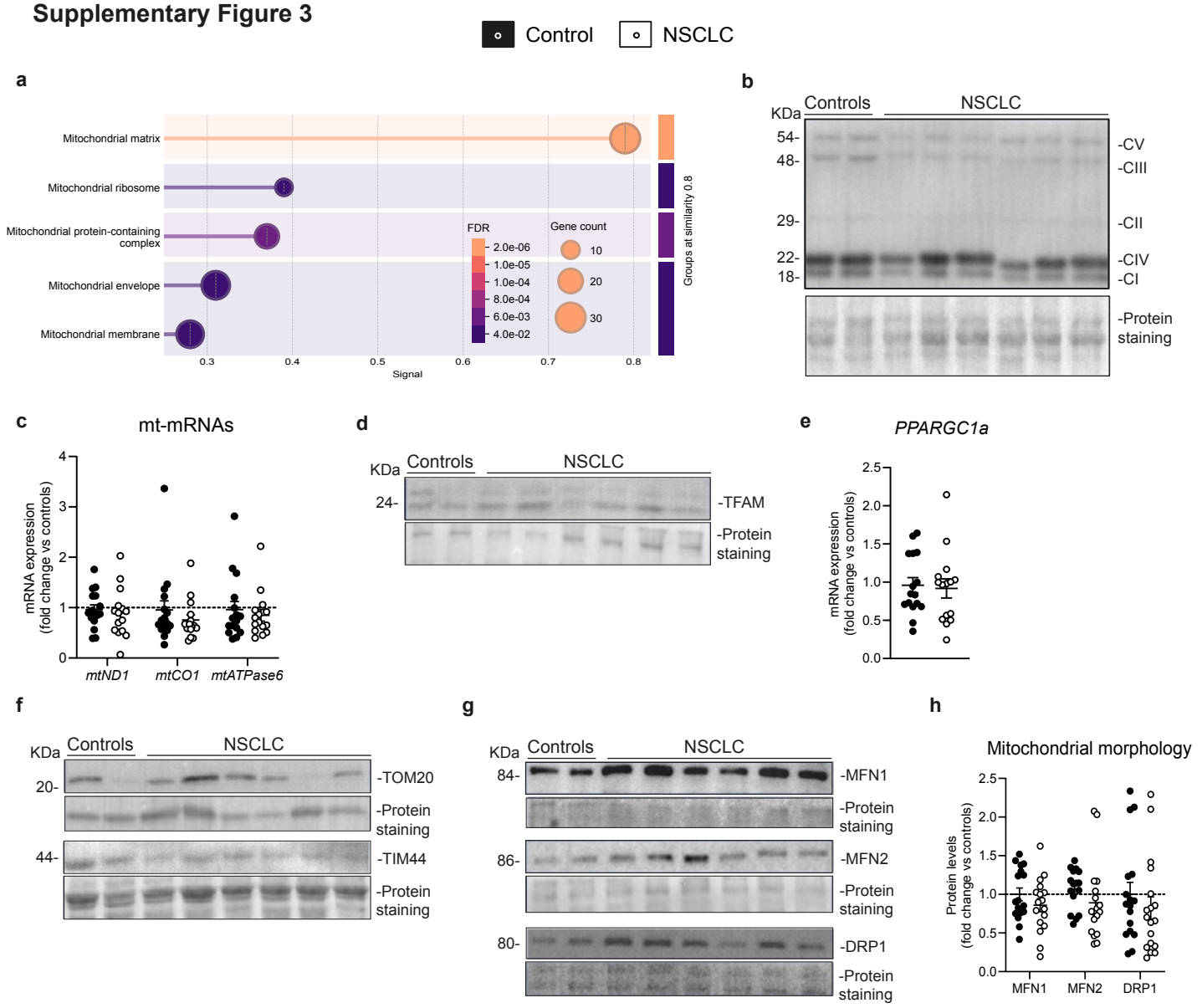

Supplementary Figure 4

Control NSCLC

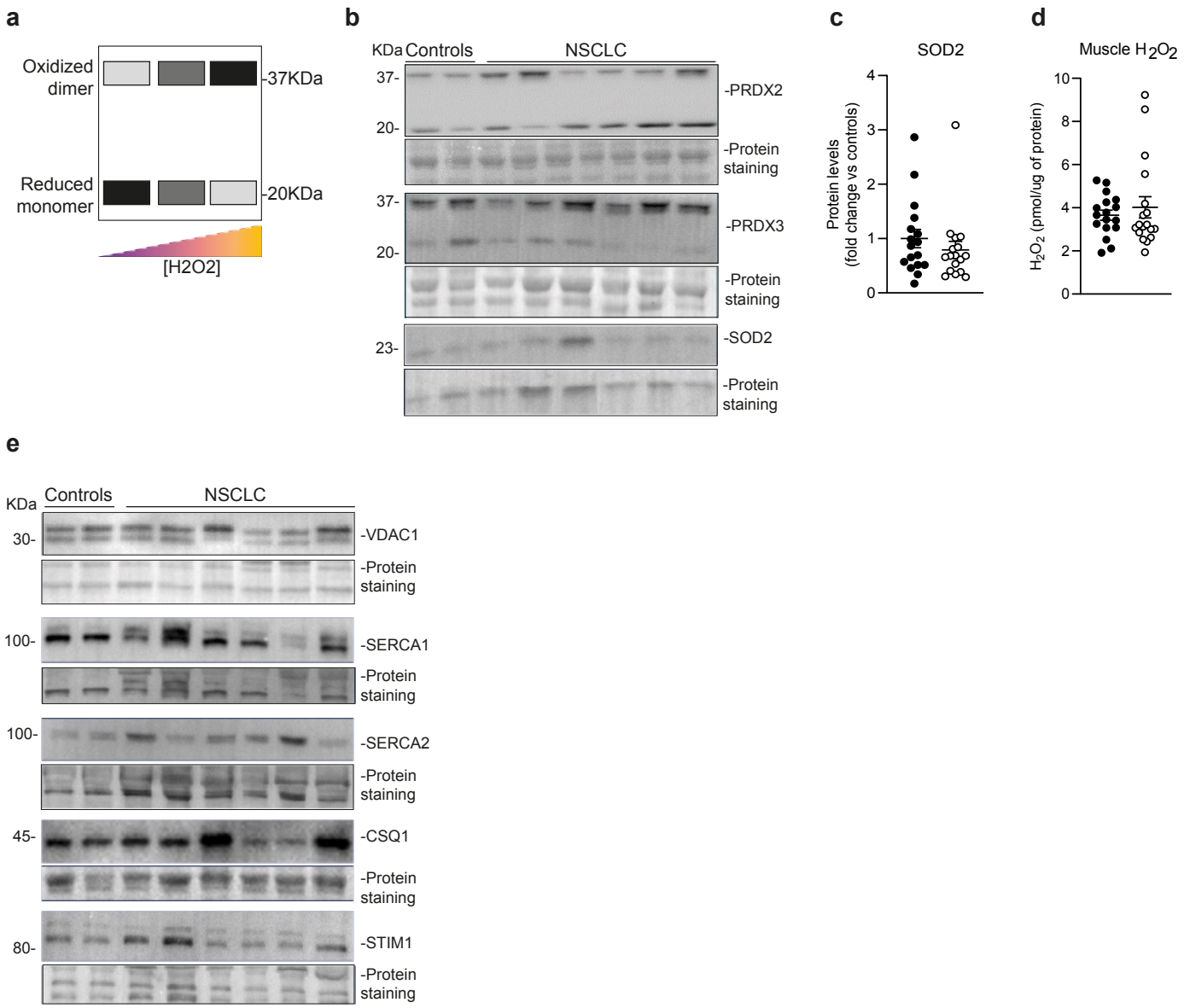
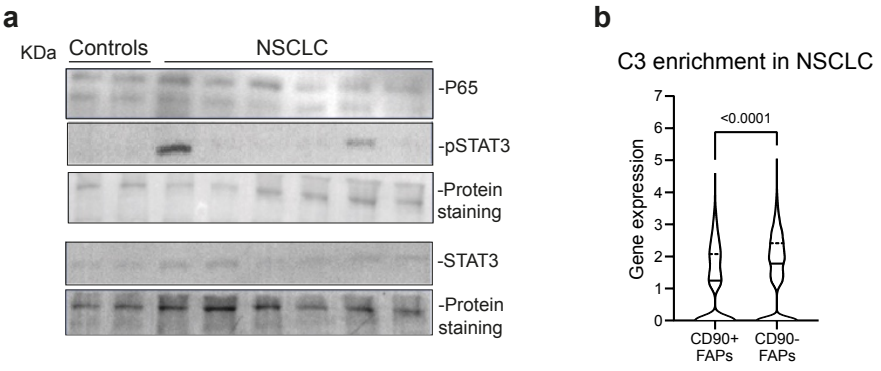
Supplementary Figure 5